



ROYAL INSTITUTE  
OF TECHNOLOGY

# Investigation of Thermal Mixing Using OpenFOAM

REIJO PEGONEN

Master Thesis  
KTH, 2012

TRITA-FYS 2012:48  
ISSN 0280-316X  
ISRN KTH/FYS/--12:48--SE

Department of Physics  
School of Engineering Science  
Royal Institute of Technology (KTH)  
AlbaNova University Center  
SE-106 91 Stockholm, Sweden

Akademisk avhandling som med tillstånd av Kungl Tekniska högskolan framlägges till offentlig granskning för avläggande av teknisk masterexamen torsdagen den 15 juni 2012 i AlbaNova Universitetscentrum, Kungl Tekniska högskolan, Roslagstullsbacken 21, Stockholm.

© Reijo Pegonen, June 2012  
Supervisors: Nicolas Forsberg, Kristian Angele and Henryk Anglart

Tryck: Universitetsservice US AB

## Abstract

During recent years, thermal mixing and thermal fatigue has received significant attention within the nuclear industry since the phenomena has led to component failures. The purpose of this Master Thesis is to make preparatory simulations for the thermal mixing experiment that will be performed at the Royal Institute of Technology within the THEMFE project. The aim is to verify that the proposed geometry and the flow conditions of the experiment will lead to low frequent temperature oscillations of the order of 0.1-1 Hz as seen in previous experiments. Such low frequencies are typical for thermal fatigue. The THEMFE experiment is a simplification of a reactor control rod. The proposed geometry consists of a top-tube and control rod stem. Both the top-tube and the control rod are cylindrical in shape. In addition there are only two hot inlet jets and two cold ones.

Thermal mixing is studied by using a transient Computational Fluid Dynamics solver for the incompressible filtered Navier-Stokes equations, namely Large Eddy Simulations in OpenFOAM. The study focuses on the region near the control rod stem. Therefore a refined grid is used in that region. During the simulations 208 processor cores are utilized.

The results reveal indeed low frequent temperature oscillations in the lower part of the mixing region near the control rod stem. The present results verify that the proposed geometry and flow conditions can be applied in the THEMFE experiment.

This work is carried out within the framework of DKC-TS, Distribuerat Kompetenscentra - Termohydraulik och Strömning, Vattenfall's initiative to exchange knowledge and experiences between nuclear units within the area of thermal hydraulics and fluid mechanics.

**Keywords:** Thermal mixing, Mixing region, Low frequency temperature oscillations, Computational Fluid Dynamics, Large Eddy Simulation, Incompressible flow.



# Acknowledgements

First of all, I would like to thank Associate Professor Henryk Anglart for accepting me as his student in the Nuclear Reactor Technology division at the KTH.

Secondly, I would like to express my sincere gratitude to my three supervisors, Nicolas Forsberg (Forsmarks Kraftgrupp AB), Kristian Angele (Vattenfall AB) and Henryk Anglart, for their continuous guidance, time, support, and constructive criticism. I could not imagine to have better supervisors and mentors for my Master Thesis.

This work is carried out within the framework of DKC-TS, Distribuerat Kompetenscentra - Termohydraulik och Strömning, Vattenfall's initiative to exchange knowledge and experiences between nuclear units within the area of thermal hydraulics and fluid mechanics.

I am grateful to Forsmarks Kraftgrupp AB for the opportunity to conduct the thesis project and for the financial support. Especially I would like to thank the FTM group for the friendly atmosphere, the inspiring discussions, and for providing the necessary computer resources.

I would like to show my gratitude to all my colleagues at the KTH Nuclear Reactor Technology division, especially to Roman Thiele for the useful consultations concerning OpenFOAM before the start of this thesis work.

Finally, I thank my wonderful parents.

June 2012

Reijo Pegonen





# Contents

|  |             |
|--|-------------|
| <b>Acknowledgements</b>  | <b>v</b>    |
| <b>Contents</b>  | <b>vii</b>  |
| <b>List of Figures</b>   | <b>ix</b>   |
| <b>List of Tables</b>  | <b>xi</b>   |
| <b>Nomenclature</b>  | <b>xiii</b> |
| <b>1 Introduction</b>  | <b>1</b>    |
| <b>2 Review of the Previous Experiment</b>                     | <b>3</b>    |
| <b>3 Theoretical Background</b>                                | <b>5</b>    |
| 3.1 Conservation of Mass . . . . .                             | 5           |
| 3.2 Conservation of Momentum . . . . .                         | 5           |
| 3.3 Conservation of Energy . . . . .                           | 6           |
| 3.4 The Boussinesq Approximation . . . . .                     | 7           |
| 3.5 Turbulence Modeling . . . . .                              | 9           |
| <b>4 The Choice of Turbulence Model</b>                        | <b>13</b>   |
| <b>5 Methodology</b>   | <b>15</b>   |
| 5.1 Geometry . . . . .   | 15          |
| 5.2 Mesh . . . . .   | 16          |
| 5.3 CFD Simulation . . . . .                                   | 18          |
| 5.4 Analysis of probed data . . . . .                          | 22          |
| 5.5 Flow through time . . . . .                                | 27          |
| <b>6 Results and Discussion</b>                                | <b>29</b>   |
| 6.1 First case, with the cold flow coming from below . . . . . | 29          |
| 6.2 Second case, with the cold inlets from the sides . . . . . | 36          |
| 6.3 The most dangerous region . . . . .                        | 41          |

|   |           |
|---|-----------|
| 6.4 Constant transport properties . . . . . | 41        |
| <b>7 Conclusions</b>                        | <b>43</b> |
| <b>Bibliography</b>                         | <b>45</b> |
| <b>A Control rod</b>                        | <b>49</b> |
| <b>B Geometry of the first case</b>         | <b>51</b> |
| <b>C Geometry of the second case</b>        | <b>53</b> |
| <b>D Mesh</b>                               | <b>55</b> |
| <b>E Inlet velocity profiles</b>            | <b>61</b> |



# List of Figures

|     |  |    |
|-----|--|----|
| 2.1 | Previous experimental results . . . . .  | 3  |
| 5.1 | Quarter geometry . . . . .   | 15 |
| 5.2 | Overview of OpenFOAM structure . . . . .   | 18 |
| 5.3 | OpenFOAM case directories . . . . .  | 19 |
| 5.4 | Probe locations . . . . .  | 22 |
| 5.5 | First case time series of the relative mean temperature change at the vertical position $y = 0.45848$ m at the different probing locations. . . . .  | 24 |
| 5.6 | Second case time series of the relative mean temperature change at the vertical position $y = 0.45848$ m at the different probing locations. . . . . | 24 |
| 5.7 | Mean temperature for different grids 1 mm from the stem wall. . . . .  | 25 |
| 5.8 | Over/under prediction compared with the thesis case. . . . .   | 26 |
| 5.9 | Temperature standard deviation for different grids 1 mm from the stem wall. . . . .  | 26 |
| 6.1 | First case time series of the temperature 1 mm from the control rod stem at the different vertical positions at the probing location "N". . . . .    | 31 |
| 6.2 | First case time series of the temperature at the vertical position $y = 0.39018$ m at the different probing locations. . . . .                       | 32 |
| 6.3 | First case mean temperature at the different probing locations. . . . .  | 33 |
| 6.4 | First case normalized temperature standard deviation at the different probing locations. . . . .   | 33 |
| 6.5 | First case temperature Fourier spectrum at the vertical position $y = 0.39018$ m at the different probing locations. . . . .                         | 34 |
| 6.6 | "Heat bullet" at the vertical positions $y = 0.39018$ m at the simulation time $t = 34.8$ s. . . . .   | 34 |
| 6.7 | The time series of the flow movement in the annulus at the vertical positions $y = 0.39018$ m. . . . .   | 35 |
| 6.8 | Second case time series of the temperature at the vertical position $y = 0.39018$ m at the different probing locations. . . . .                      | 37 |
| 6.9 | Second case mean temperature at the different probing locations. . . . .   | 38 |

|      |   |    |
|------|---|----|
| 6.10 | Second case normalized temperature standard deviation at the different probing locations. . . . .                           | 38 |
| 6.11 | Second case temperature Fourier spectrum at the vertical position $y=0.39018$ m at the different probing locations. . . . . | 39 |
| 6.12 | Normalized temperature standard deviation comparison at the probing location "N". . . . .                                   | 39 |
| 6.13 | Visualization of the region where the temperature increases rapidly from 333 to 520 K. . . . .                              | 40 |
| A.1  | Control rod with welded connection between blades and stem . . . . .  | 49 |
| B.1  | Isometric view of the first case geometry . . . . .   | 51 |
| B.2  | Dimensions of the first case geometry . . . . .   | 52 |
| C.1  | Isometric view of the second case geometry . . . . .  | 53 |
| C.2  | Dimensions of the second case geometry . . . . .  | 54 |
| D.1  | Top view of the mesh . . . . .  | 55 |
| D.2  | Zoomed top view of the mesh . . . . .   | 56 |
| D.3  | Side view of the mesh . . . . .   | 57 |
| D.4  | Cut view of the inlets from above . . . . .   | 58 |
| D.5  | Cut view of the inlet from symmetry plane . . . . .   | 59 |
| D.6  | Hexahedron skewness . . . . .   | 60 |
| E.1  | Radial velocity profile for hot inlet . . . . .   | 61 |
| E.2  | Radial velocity profile for cold inlet . . . . .  | 62 |

# List of Tables

|     |  |    |
|-----|--|----|
| 5.1 | Mesh information . . . . .                         | 16 |
| 5.2 | Mesh quality (skewness) . . . . .                  | 17 |
| 5.3 | SIMPLE and PISO algorithm . . . . .                | 19 |
| 5.4 | Boundary conditions . . . . .                      | 20 |
| 5.5 | Discretization and interpolation schemes . . . . . | 21 |
| 5.6 | Grid dependence study meshes . . . . .             | 25 |
| 6.1 | Water properties . . . . .                         | 42 |



# Nomenclature

## Dimensionless Symbols

|               |                             |
|---------------|-----------------------------|
| $\delta_{ij}$ | Kronecker delta             |
| $Co$          | Courant number              |
| $Pr$          | Prandtl number              |
| $Pr_{SGS}$    | SGS Prandtl number          |
| $Pr_t$        | Turbulent Prandtl number    |
| $Re$          | Reynolds number             |
| $Ri$          | Richardson number           |
| $T^*$         | Non-dimensional temperature |

## Greek Symbols

|                |                                   |                           |
|----------------|-----------------------------------|---------------------------|
| $\alpha$       | Thermal diffusivity               | $[m^2/s]$                 |
| $\alpha_{eff}$ | Effective thermal diffusivity     | $[m^2/s]$                 |
| $\alpha_\rho$  | Coefficient of thermal expansion  | $[K^{-1}]$                |
| $\beta_\rho$   | Isothermal compressibility        | $[Pa^{-1}]$               |
| $\epsilon$     | Kinetic energy dissipation rate   | $[m^2/s^3]$               |
| $\lambda$      | Thermal conductivity              | $[J/(m \cdot s \cdot K)]$ |
| $\lambda_t$    | Turbulent thermal conductivity    | $[J/(m \cdot s \cdot K)]$ |
| $\mu$          | Dynamic viscosity                 | $[Pa \cdot s]$            |
| $\nu$          | Kinematic viscosity               | $[m^2/s]$                 |
| $\nu_{eff}$    | Effective kinematic viscosity     | $[m^2/s]$                 |
| $\nu_{SGS}$    | SGS kinematic viscosity           | $[m^2/s]$                 |
| $\nu_t$        | Turbulence kinematic viscosity    | $[m^2/s]$                 |
| $\Theta$       | SGS heat flux                     | $[K \cdot m/s]$           |
| $\rho$         | Density                           | $[kg/m^3]$                |
| $\sigma$       | Stress tensor                     | $[Pa]$                    |
| $\sigma_T$     | Standard deviation of temperature | $[K]$                     |
| $\tau$         | Viscous stress tensor             | $[Pa]$                    |
| $\tau^R$       | Reynolds stress tensor            | $[m^2/s^2]$               |
| $\tau^{SGS}$   | Sub-grid-scale stress tensor      | $[m^2/s^2]$               |

**Roman Letters**

|            |                                   |                    |
|------------|-----------------------------------|--------------------|
| $c_p$      | Specific heat capacity            | $[J/(kg \cdot K)]$ |
| $e$        | Specific total energy             | $[J/kg]$           |
| $f$        | Total body acceleration           | $[m/s^2]$          |
| $f$        | Frequency                         | $[Hz]$             |
| $g$        | Gravitational acceleration        | $[m/s^2]$          |
| $k$        | Specific kinetic energy           | $[J/kg]$           |
| $k_{SGS}$  | Specific SGS kinetic energy       | $[J/kg]$           |
| $k_t$      | Specific turbulent kinetic energy | $[J/kg]$           |
| $p$        | Pressure                          | $[Pa]$             |
| $q''$      | Conductive heat flux              | $[J/m^2]$          |
| $q'''$     | Volumetric heat source            | $[J/m^3]$          |
| $t$        | Time                              | $[s]$              |
| $T$        | Temperature                       | $[K]$              |
| $T_{cold}$ | Temperature of cold inlet         | $[K]$              |
| $T_{hot}$  | Temperature of hot inlet          | $[K]$              |
| $T_t$      | Time interval                     | $[s]$              |
| $u$        | Specific internal energy          | $[J/kg]$           |
| $v$        | Velocity                          | $[m/s]$            |
| $x_i$      | Position vector component         | $[m]$              |

**Abbreviations**

|        |  |
|--------|--|
| CFD    | Computational Fluid Dynamics                       |
| LES    | Large Eddy Simulations                             |
| PISO   | Pressure Implicit with Splitting of Operators      |
| RANS   | Raynolds-Averaged Navier-Stokes                    |
| SGS    | Sub-Grid-Scale                                     |
| SIMPLE | Semi-Implicit Method for Pressure-Linked Equations |

# Chapter 1

## Introduction

Turbulent mixing of two streams with different temperature can cause temperature fluctuations that may lead to thermal fatigue. Thermal fatigue has received increasing attention in recent years in the nuclear industry due to component failures. Control rod drive problems were observed during the refueling outage of Unit 3 of Oskarshamn Nuclear Power Plant in Sweden in October 2008 [7, 25]. A crack at the welded joint at the control rod stem was discovered (Figure A.1) [25]. This led to inspections by the Swedish Radiation Safety Authority (SSM) at all remaining control rods at Oskarshamn 3 and at its "twin" reactor Forsmark 3. Results from Forsmark 3 revealed that about 25% of the 197 checked control rod drives were found to have crevices or relevant cracks and one was broken [7]. Cracks that were found at the upper part of the stem of many control rods is believed to originate from thermal fatigue that is caused by mixing of cold laminar crud flow in the annular gap between the control rod stem and the top tube (60°C) and hot turbulent bypass flow (276°C), forming jets through holes in the guide tube [25].

This master thesis is one part of a thermal mixing experiment that will be performed by the Nuclear Reactor Technology (NRT) Division at the Royal Institute of Technology (KTH) in Sweden. The project is called THEMFE (Thermal Mixing and Fatigue Experiment) and was initiated by: SSM, Forsmarks Kraftgrupp AB, Ringhals AB, Oskarshamns Kraftgrupp AB and Teollisuuden Voima Oyj (TVO). The aim of THEMFE is to obtain experimental data to predict heat transfer. These data are used to benchmark Computational Fluid Dynamic (CFD) calculations. The aim of this master thesis is to make preparatory simulations for the experiment using the open-source CFD code OpenFOAM®. The geometry in THEMFE is a simplified control rod, top-tube and guide tube geometry with only two upper and two lower by-pass inlets. The complex geometry is significantly simplified. The geometry used in this thesis is further simplified, in order to mainly model the mixing region and to study it more closely. All the simplifications are done in a way to preserve the relevant physics of the thermal mixing. The goal of these simulations

is to verify that the proposed geometry will give rise to low frequent oscillations (of the order of 0.1-1 Hz). These oscillations are considered to be responsible for the control rod drive thermal fatigue and the results of this thesis work will be used for deciding on the experimental setup and experimental conditions.

Previous CFD simulations done in Forsmark on the real control rod geometry showed that the temperature is oscillating in the mixing region with a frequency varying from 0.01 Hz to 1 Hz and that the fluctuations are triggered by eddies coming from the upper warm water bypass flow inlets [2, 25].

During this thesis the following programs were used: SolidWorks for creating geometries, ANSYS ICEM 14 for making the structured mesh, OpenFOAM for CFD simulations, ParaView and MATLAB for post-processing and finally L<sup>A</sup>T<sub>E</sub>X with TeXnicCenter for writing this thesis. Forsmarks Kraftgrupp AB's computational cluster was used for the OpenFOAM simulations. During the run of thesis cases 208 processor cores were used, total CPU time was 1.2 thousand hours.

This thesis will start with a review of the previous experiment performed at Vattenfall Research & Development AB, followed by the Theoretical Background, The Choice of Turbulence Model, Methodology, Results and Discussion and finally Conclusions.

This work is carried out within the framework of DKC-TS, Distribuerat Kompetenscentra - Termohydraulik och Strömning, Vattenfall's initiative to exchange knowledge and experiences between nuclear units within the area of thermal hydraulics and fluid mechanics.



## Chapter 2

# Review of the Previous Experiment

In the previous work, by Vattenfall Research & Development AB, an experiment was carried out to study the thermal mixing in the annular gap between the guide tube and the control rod stem. The experiment revealed a characteristic temperature fluctuation in the mixing region that can be seen in Figure 2.1 [2].

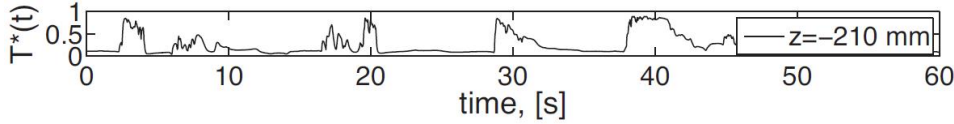


Figure 2.1: Previous experimental results: Time series of the temperature 1 mm from the control rod stem in the mixing region 210 mm vertically upstream of the lower bypass inlets. [2]

In Figure 2.1  $T^*$  denotes the non-dimensional temperature defined as:

$$T^* = \frac{T - T_{cold}}{T_{hot} - T_{cold}}, \quad (2.1)$$

where  $T_{hot}$  and  $T_{cold}$  are the temperatures of the hot and the cold inlets. In [2] the thermal fluctuations were given the following characteristics:

- The maximum amplitude of the fluctuations is almost as large as the total temperature difference between the cold and the hot inlet (In Figure 2.1  $T^*$  is fluctuating almost between 0 and 1).
- The temperature fluctuations are characterized by low frequencies of the order of 0.1-1 Hz.

- When the hot water penetrates the annular gap the temperature is increasing rapidly and then gradually decreasing when mixed with the cold flow (Figure 2.1).

The characteristic shape of the temperature time traces (in Figure 2.1 between 28 and 32 s) was caused by "heat bullets" (the stipulative definition, used by the author of this thesis, of a hot inlets jets penetrating into the colder flow). The hot jet, after hitting the control rod stem wall, penetrates into the colder flow and pushes it backwards creating a mixing region. The "heat bullet" is responsible for the local instantaneous temperature change from  $T_{cold}$  to practically  $T_{hot}$  at a fixed position close to the control rod stem. After reaching nearly  $T_{hot}$  the temperature gradually decreases to its initial cold value. Additionally it was observed that the larger the temperature difference between the hot and the cold inlet flows, the shorter the length of the mixing region [2]. This is because of the larger density difference, which makes it more difficult for the hot water to penetrate the cold.

## Chapter 3

# Theoretical Background

This chapter summarizes what is explained in more detailed in [3] and [9]. The aim is to remind the reader of the equations for single-phase incompressible isothermal flow, i.e. when density is considered to be constant. In addition a short overview of the Boussinesq approximation and turbulence modeling is given.

### 3.1 Conservation of Mass

The continuity equation for single-phase, one component flows expressed on differential form is:

$$\frac{\partial \rho}{\partial t} + \nabla \cdot (\rho \mathbf{v}) = \frac{\partial \rho}{\partial t} + \rho \frac{\partial v_i}{\partial x_i} = 0, \quad (3.1)$$

where  $v$  is the velocity and  $\rho$  the density. By assuming constant density in time and space the mass conservation equation simplifies to:

$$\nabla \cdot \mathbf{v} = \frac{\partial v_i}{\partial x_i} = 0. \quad (3.2)$$

### 3.2 Conservation of Momentum

The momentum conservation equation for single-phase flows expressed on differential form:

$$\rho \frac{\partial v_i}{\partial t} + \rho \frac{\partial (v_j v_i)}{\partial x_j} = - \frac{\partial p}{\partial x_i} + \frac{\partial \tau_{ij}}{\partial x_j} + \rho f_i, \quad (3.3)$$

where  $p$  is the pressure,  $\tau$  is the viscous stress tensor and  $f$  is the total body acceleration. Here the left hand side of the equation represents acceleration and advection and the first two terms on the right hand side are the gradient of pressure and of shear stress tensor. The first two terms on the right right hand side are surface forces and the third is volume force.

For a Newtonian fluid the viscous stress is given by:

$$\tau_{ij} = \mu \left( \frac{\partial v_i}{\partial x_j} + \frac{\partial v_j}{\partial x_i} \right) - \frac{2}{3} \mu \frac{\partial v_k}{\partial x_k} \delta_{ij}, \quad (3.4)$$

where  $\mu$  is the dynamic viscosity and  $\delta_{ij}$  is the Kronecker delta. For incompressible flows the last term in equation (3.4) is zero. By combining equations (3.2) - (3.4) the *Navier-Stokes* momentum equation for incompressible flows is obtained:

$$\rho \frac{\partial v_i}{\partial t} + \rho v_j \frac{\partial v_i}{\partial x_j} = -\frac{\partial p}{\partial x_i} + \frac{\partial}{\partial x_j} \left[ \mu \left( \frac{\partial v_i}{\partial x_j} + \frac{\partial v_j}{\partial x_i} \right) \right] + \rho f_i. \quad (3.5)$$

### 3.3 Conservation of Energy

The transport equation for the specific kinetic energy  $k$  ( $k = v_i v_i / 2$ ) is obtained by multiplying equation (3.3) with  $v_i$ :

$$v_i \rho \frac{Dv_i}{Dt} = v_i \rho \frac{\partial v_i}{\partial t} + v_i \rho \frac{\partial (v_j v_i)}{\partial x_j} = -v_i \frac{\partial p}{\partial x_i} + v_i \frac{\partial \tau_{ij}}{\partial x_j} + v_i \rho f_i. \quad (3.6)$$

The left hand side can be re-written as:

$$v_i \rho \frac{Dv_i}{Dt} = \frac{\rho}{2} \frac{D(v_i v_i)}{Dt} = \rho \frac{Dk}{Dt} \quad (3.7)$$

and the transport equation for the specific kinetic energy can be written as:

$$\rho \frac{Dk}{Dt} = -v_i \frac{\partial p}{\partial x_i} + v_i \frac{\partial \tau_{ij}}{\partial x_j} + v_i \rho f_i. \quad (3.8)$$

Now the transport equation for the specific internal energy  $u$  is used:

$$\rho \frac{Du}{Dt} = -p \frac{\partial v_i}{\partial x_i} + \tau_{ij} \frac{\partial v_i}{\partial x_j} - \frac{\partial q_i''}{\partial x_i} + q''', \quad (3.9)$$

where  $q''$  is the conductive heat flux and  $q'''$  is the volumetric heat source. By adding equations (3.8) and (3.9) the transport equation for the specific total energy  $e = k + u$  is formed:

$$\rho \frac{De}{Dt} = \rho \frac{D(k+u)}{Dt} = \frac{\partial (v_i \sigma_{ij})}{\partial x_j} - \frac{\partial q_i''}{\partial x_i} + q''' + v_i \rho f_i, \quad (3.10)$$

$$\sigma_{ij} = -p \delta_{ij} + \tau_{ij}, \quad (3.11)$$

where  $\sigma$  is the stress tensor. Next it is possible to get the temperature equation. Using Fourier's law:

$$q_i'' = -\lambda \frac{\partial T}{\partial x_i}, \quad (3.12)$$

where  $\lambda$  is the thermal conductivity and  $T$  the temperature, in combination with the conservation of mass equation (3.2) and the relationship [3]:

$$\frac{Du}{Dt} = \frac{D(c_p T)}{Dt} - \frac{\alpha_\rho T}{\rho} \frac{Dp}{Dt} - \frac{p}{\rho} \frac{\partial v_i}{\partial x_i}, \quad (3.13)$$

where  $c_p$  is the specific heat capacity and  $\alpha_\rho$  is the coefficient of thermal expansion, and equation (3.9) the following is obtained:

$$\rho \frac{D(c_p T)}{Dt} = \tau_{ij} \frac{\partial v_i}{\partial x_j} + \alpha_\rho T \frac{Dp}{Dt} - \frac{\partial}{\partial x_i} \left( -\lambda \frac{\partial T}{\partial x_i} \right) + q'''. \quad (3.14)$$

Assuming that there is no heat source and that the specific heat capacity and the thermal conductivity are constant equation (3.14) simplifies to:

$$\rho c_p \frac{DT}{Dt} = \tau_{ij} \frac{\partial v_i}{\partial x_j} + \alpha_\rho T \frac{Dp}{Dt} + \lambda \frac{\partial^2 T}{\partial x_i \partial x_i}. \quad (3.15)$$

The first two terms on the right hand side of the equation can be neglected for an incompressible and Newtonian fluid [9]. Finally the temperature equation is expressed as:

$$\frac{DT}{Dt} = \frac{\nu}{Pr} \frac{\partial^2 T}{\partial x_i \partial x_i}, \quad (3.16)$$

since the Prandtl number is defined as:

$$Pr = \frac{\nu}{\alpha}, \quad (3.17)$$

where  $\alpha$  is the thermal diffusivity:

$$\alpha = \frac{\lambda}{\rho c_p}. \quad (3.18)$$

### 3.4 The Boussinesq Approximation

In 1903 Joseph Valentin Buossinesq (13 March 1842 - 19 February 1929) wrote:

"One still had to observe that in most heat-induced motions of our heavy fluids, the volumes or densities are approximately conserved, although the corresponding variation of the weight of the unit of volume is actually the cause of the phenomena we are studying. One possibility stems from there: neglecting the variations of the density where they are not multiplied by the gravity  $g$ , while conserving its product by the gravity in the calculations." [5]

and

"The weight  $\rho g$  of the unit of volume [ . . . ] will have approximately decreased of the quantity  $\rho g \alpha \theta$ , as if a small antagonistic [i.e. ascensional] force proportional to the temperature difference  $\theta$ , but in the upward direction, had added itself to the initial or normal weight of the unit of volume." [5]

These sentences formulated the Buossinesq approximation that is commonly understood to consist of the following [15]:

- Density is assumed constant except when it directly causes buoyancy forces;
- All other fluid properties are assumed constant;
- Viscous dissipation is assumed negligible.

The density multiplied with the gravitational acceleration  $g$  is approximated with [15]:

$$\rho g_i = \rho_0 [1 - \alpha_{\rho,0}(T - T_0) + \beta_{\rho,0}(p - p_0)] g_i, \quad (3.19)$$

where

$$\alpha_\rho = -\frac{1}{\rho} \frac{\delta \rho}{\delta T}, \quad (3.20)$$

$$\beta_\rho = -\frac{1}{\rho} \frac{\delta \rho}{\delta p}, \quad (3.21)$$

where  $\alpha_\rho$  is the coefficient of thermal expansion and  $\beta_\rho$  is the isothermal compressibility.  $\alpha_{\rho,0}$  and  $\beta_{\rho,0}$  means that  $\alpha_\rho$  and  $\beta_\rho$  are calculated at reference state  $(T_0, p_0)$ .  $T_0$ ,  $p_0$ ,  $\rho_0$  are reference temperature, pressure and density. In equation (3.19) the third term on the right hand side can be neglected, because of the estimation  $\frac{\alpha_{\rho,0}(T-T_0)}{\beta_{\rho,0}(p-p_0)} > 10^4$ . The buoyancy effect can be taken into account by using the Boussinesq approximation with equations (3.3) and (3.10). At first all equations are divided with  $\rho_0$  and then density differences are neglected in all terms except in the body force term where approximation (3.19) is used. The following equations are obtained after these manipulations:

$$\frac{\partial v_i}{\partial t} + \frac{\partial(v_j v_i)}{\partial x_j} = -\frac{1}{\rho_0} \frac{\partial p}{\partial x_i} + \frac{1}{\rho_0} \frac{\partial \tau_{ij}}{\partial x_j} + [1 - \alpha_{\rho,0}(T - T_0)] g_i, \quad (3.22)$$

$$\frac{de}{dt} = \frac{1}{\rho_0} \frac{\partial(v_i \sigma_{ij})}{\partial x_j} - \frac{1}{\rho_0} \frac{\partial q_i''}{\partial x_i} + \frac{q'''}{\rho_0} + v_i [1 - \alpha_{\rho,0}(T - T_0)] g_i, \quad (3.23)$$

where we have made the assumption that the only active volume force is buoyancy, hence  $f_i = g_i$ .

### 3.5 Turbulence Modeling

In turbulence modeling the dependent variables are decomposed into two parts, one averaged or filtered ( $\bar{\Phi}$ ), one fluctuating or sub-grid-scale ( $\Phi'$ ) [9]:

$$\Phi = \bar{\Phi} + \Phi'. \quad (3.24)$$

The second term on the right hand side can represent either time averaging or spatial filtering. The time average of a variable  $\Phi$  can be found by evaluating the following integral:

$$\bar{\Phi}(\mathbf{x}) = \lim_{T_t \rightarrow \infty} \frac{1}{T_t} \int_0^{T_t} \Phi(\mathbf{x}, t) dt, \quad (3.25)$$

here  $T_t$  is the time interval. The time averaging has following properties [14]:

$$\overline{\Phi'} = 0, \quad (3.26)$$

$$\overline{\bar{\Phi}} = \bar{\Phi}, \quad (3.27)$$

$$\frac{\partial}{\partial t} \bar{\Phi} = \overline{\frac{\partial \Phi}{\partial t}} = 0. \quad (3.28)$$

The *Reynolds-Averaged Navier-Stokes (RANS)* equations are obtained by applying (3.25) on incompressible Navier-Stokes equations and averaging the entire equations:

$$\frac{\partial \bar{v}_i}{\partial x_i} = 0, \quad (3.29)$$

$$\rho \bar{v}_j \frac{\partial \bar{v}_i}{\partial x_j} = -\frac{\partial \bar{p}}{\partial x_i} + \frac{\partial \bar{\tau}_{ij}}{\partial x_j} - \rho \frac{\partial \tau_{ij}^R}{\partial x_j} + \rho \bar{f}_i, \quad (3.30)$$

where the following was used [14]:

$$\overline{v_i v_j} = \bar{v}_i \bar{v}_j + \overline{v'_i v'_j} = \bar{v}_i \bar{v}_j - \tau_{ij}^R, \quad (3.31)$$

where  $\tau_{ij}^R$  is the Reynolds stress tensor.  $\tau_{ij}^R$  can be evaluated by using the Boussinesq assumption that the stress tensor is linear to the mean strain rate tensor [14]:

$$\tau_{ij}^R = -\nu_t \left( \frac{\partial \bar{v}_i}{\partial x_j} + \frac{\partial \bar{v}_j}{\partial x_i} \right) + \frac{2}{3} k_t \delta_{ij}, \quad (3.32)$$

where  $\nu_t$  is the turbulence kinematic viscosity or eddy viscosity,  $k_t = \overline{v_i v_i}/2$  is the specific turbulent kinetic energy. For incompressible flows last term in equation (3.32) is zero. There are many different models to calculate  $\nu_t$  used in RANS. One possibility is to use the standard  $k$ - $\epsilon$  model, where  $\nu_t$  is expressed as [9]:

$$\nu_t = C_\mu \frac{k_t^2}{\epsilon}, \quad (3.33)$$

and to close unknowns variables  $k_t$  and  $\epsilon$  [14]:

$$\frac{\partial k_t}{\partial t} + \overline{v_j} \frac{\partial k_t}{\partial x_j} = \frac{\partial}{\partial x_i} ((\nu + \nu_t) \frac{\partial k_t}{\partial x_i}) + \nu_t \overline{S^2} - \epsilon, \quad (3.34)$$

$$\frac{\partial \epsilon}{\partial t} + \overline{v_j} \frac{\partial \epsilon}{\partial x_j} = \frac{\partial}{\partial x_i} ((\nu + \nu_t) \frac{\partial \epsilon}{\partial x_i}) + \frac{C_{\epsilon 1} \nu_t \overline{S^2} \epsilon}{k_t} - \frac{C_{\epsilon 2} \epsilon^2}{k_t}, \quad (3.35)$$

here  $\epsilon$  denotes the kinetic energy dissipation rate,  $C_\mu=0.09$ ,  $C_{\epsilon 1} = 1.44$ ,  $C_{\epsilon 2} = 1.92$  and  $S = \sqrt{2S_{ij}S_{ij}}$  is the modulus of the mean rate-of-strain stress:

$$S_{ij} = \frac{1}{2} \left( \frac{\partial v_i}{\partial x_j} - \frac{\partial v_j}{\partial x_i} \right). \quad (3.36)$$

In spatial filtering  $\overline{\Phi}$  is defined as:

$$\overline{\Phi}(\mathbf{x}_0, t) = \int_{\Omega} \Phi(\mathbf{x}, t) G(\mathbf{x}_0, \mathbf{x}, \Delta) d\mathbf{x}, \quad (3.37)$$

where  $G(\mathbf{x}_0, \mathbf{x}, \Delta)$  is the spatial filter,  $\Delta$  the filter size and  $\Omega$  the entire space. Generally OpenFOAM uses tophat spatial filter:

$$G(\mathbf{x}_0, \mathbf{x}, \Delta) = \begin{cases} 1/\Delta^3 & |\mathbf{x}_0 - \mathbf{x}| \leq \Delta/2 \\ 0 & otherwise \end{cases} \quad (3.38)$$

In spatial filtering we have the following properties [14]:

$$\overline{\Phi'} \neq 0, \quad (3.39)$$

$$\overline{\overline{\Phi}} \neq \overline{\Phi}. \quad (3.40)$$

The *Large Eddy Simulation (LES)* equations are obtained by applying (3.37) on incompressible Navier-Stokes equations and filtering the entire equations:

$$\frac{\partial \overline{v_i}}{\partial x_i} = 0, \quad (3.41)$$

$$\rho \frac{\partial \overline{v_i}}{\partial t} + \rho \overline{v_j} \frac{\partial (\overline{v_i})}{\partial x_j} = - \frac{\partial \overline{p}}{\partial x_i} + \frac{\partial \overline{\tau_{ij}}}{\partial x_j} - \rho \frac{\partial \tau_{ij}^{SGS}}{\partial x_j} + \rho \overline{f_i}, \quad (3.42)$$

where following was used[14]:

$$\overline{v_i v_j} = \overline{v_i} \overline{v_j} + \overline{v_i v'_j} + \overline{v'_i v_j} + \overline{v'_i v'_j} = \overline{v_i} \overline{v_j} - \tau_{ij}^{SGS}. \quad (3.43)$$

Equations (3.41) and (3.42) are similar to (3.29) and (3.30), except for  $\tau_{ij}^R$  is switched with  $\tau_{ij}^{SGS}$  and  $\frac{\partial \overline{v_i}}{\partial t} = 0$  in *RANS*. Equation (3.41) is valid when the filter size ( $\Delta$ ) and the filtering volume ( $\Omega$ ) are constants [9]. If they are dependent on  $x_i$  then an error of the second order is made [9]. The CFD simulations in this



work use second order numerical schemes and therefore a second order error can be accepted if the mesh quality is sufficiently fine.  $\tau_{ij}^{SGS}$  is called the sub-grid-scale stress tensor and the Boussinesq assumption of SGS stress tensor is given by [14]:

$$\tau_{ij}^{SGS} = \frac{2}{3}k_{SGS}\delta_{ij} - 2\nu_{SGS}\bar{S}_{ij} + \frac{2}{3}\nu_{SGS}\bar{S}_{kk}\delta_{ij}, \quad (3.44)$$

$$\nu_{SGS} = C_k\bar{\Delta}\sqrt{k_{SGS}}, \quad (3.45)$$

when the One Equation Eddy model is used, where  $\nu_{SGS}$  is the SGS kinematic viscosity,  $k_{SGS} = (\overline{v_i v_i} - \bar{v}_i \bar{v}_i)/2$  is the specific SGS kinetic energy and  $C_k \approx 0.07$ . When Smagorinsky model is used the sub-grid-scale stress tensor is approximated as [14]:

$$\tau_{ij}^{SGS} = -2\nu_{SGS}\bar{S}_{ij} + \frac{2}{3}\nu_{SGS}\bar{S}_{kk}\delta_{ij}, \quad (3.46)$$

$$\nu_{SGS} = (C_S\bar{\Delta})^2\bar{S}, \quad (3.47)$$

here  $C_S \approx 0.16$ . For incompressible flows last term in equations (3.44) and (3.46) is zero.

The same procedure as used for the momentum equation is used for the temperature equation to obtain the averaged equation. Equation (3.16) can be re-written as:

$$\frac{\partial T}{\partial t} + \frac{\partial(v_j T)}{\partial x_j} = \frac{\nu}{Pr} \frac{\partial^2 T}{\partial x_i \partial x_i}. \quad (3.48)$$

After substitutions  $T = \bar{T} + T'$ ,  $v_j = \bar{v}_j + v'_j$  and time averaging a new term appears:

$$\frac{\partial \bar{T}}{\partial t} + \frac{\partial(\bar{v}_j \bar{T})}{\partial x_j} = \frac{\nu}{Pr} \frac{\partial^2 \bar{T}}{\partial x_i \partial x_i} - \frac{\partial(\overline{v'_i T'})}{\partial x_i}, \quad (3.49)$$

where  $\rho c_p \overline{v'_i T'}$  is called the eddy heat flux [24]:

$$\overline{v'_i T'} = -\frac{\lambda_t}{\rho c_p} \frac{\partial \bar{T}}{\partial x_i}, \quad (3.50)$$

where  $\lambda_t$  is the turbulent thermal conductivity. Combining equations (3.49) and (3.50) Reynold-averaged temperature equation is obtained:

$$\frac{\partial \bar{T}}{\partial t} + \frac{\partial(\bar{v}_j \bar{T})}{\partial x_j} = \frac{\nu}{Pr} \frac{\partial^2 \bar{T}}{\partial x_i \partial x_i} + \frac{\lambda_t}{\rho c_p} \frac{\partial^2 \bar{T}}{\partial x_i \partial x_i}. \quad (3.51)$$

Last equation can be re-written as:

$$\frac{\partial \bar{T}}{\partial t} + \frac{\partial(\bar{v}_j \bar{T})}{\partial x_j} = \alpha_{eff} \frac{\partial^2 \bar{T}}{\partial x_i \partial x_i}, \quad (3.52)$$

where  $\alpha_{eff}$  is the effective thermal diffusivity and it is defined as:

$$\alpha_{eff} = \frac{\nu}{Pr} + \frac{\nu_t}{Pr_t}, \quad (3.53)$$

where  $\nu_t$  and  $Pr_t$  are the turbulent kinematic viscosity and the turbulent Prandtl number.

LES temperature equation is obtained in the similar way. After substitutions  $T = \bar{T} + T'$ ,  $v_j = \bar{v}_j + v'_j$  into equation (3.48) and spacial filtering following equation is obtained [6]:

$$\frac{\partial \bar{T}}{\partial t} + \frac{\partial(\bar{v}_j \bar{T})}{\partial x_j} = \frac{\nu}{Pr} \frac{\partial^2 \bar{T}}{\partial x_i \partial x_i} + \frac{\partial \Theta_i}{\partial x_i}. \quad (3.54)$$

$\Theta_i$  is the SGS heat flux [6]:

$$\Theta_i = \frac{\nu_{SGS}}{Pr_{SGS}} \frac{\partial \bar{T}}{\partial x_i}, \quad (3.55)$$

where  $Pr_{SGS}$  is the SGS Prandtl number. LES temperature equation is obtained by combining equations (3.54) and (3.55):

$$\frac{\partial \bar{T}}{\partial t} + \frac{\partial(\bar{v}_j \bar{T})}{\partial x_j} = \alpha_{eff} \frac{\partial^2 \bar{T}}{\partial x_i \partial x_i}. \quad (3.56)$$

Here the effective thermal diffusivity is defined as:

$$\alpha_{eff} = \frac{\nu}{Pr} + \frac{\nu_{SGS}}{Pr_{SGS}}. \quad (3.57)$$

## Chapter 4

# The Choice of Turbulence Model

Three turbulence models, one RANS and two LES models, were considered and comparative simulations were carried out for the choice of model. The standard  $k-\epsilon$  approach was used in RANS and in LES the One Equation Eddy model and the Smagorinski models were tested. All models were discussed in the previous chapter.

The geometry created for the choice of turbulence model was similar to that seen in Appendix B however it was 200 mm shorter (700 instead of 900 in Figure B.2). The mesh had 475 376 hexahedral cells and was created similarly as discussed in chapter 5.

With RANS at first the SIMPLE algorithm (Table 5.3) was used in order to get fully developed flow at the inlets. Steady-state simulations were done on pipe geometries, that represented only the inlets, having a length of 20 diameters. The obtained results were used as the initial conditions for the inlets in a full geometry, where the inlets were shortened to the length of two diameters. The results were mapped onto the full geometry before the PIMPLE algorithm was used (i.e. a mixture of SIMPLE and PISO, Table 5.3) for the transient simulation. The RANS transient simulation was carried out on 16 processor cores and 10.97 s of simulation time was achieved within 7 days.

With LES the PISO algorithm (Table 5.3) was used and two cases were constructed which differed in respect of the LES-models used: the One Equation Eddy model and the Smagorinski model. Flat inlet flow conditions were applied because the steady-state algorithm cannot be used with LES. The Smagorinski LES-model reached 42.6 s simulation time within 19 days while using 32 processor cores, while the One Equation Eddy model reached only 30.2 s.

After the results were analyzed, LES was picked to be used in master thesis case. There were mainly two reasons for that: the RANS averaged out unsteady turbulent

fluctuations and no temperature fluctuations in a short time scale could be observed; both LES versions showed similar behaviors. Although the One Equation Eddy and the Smagorinski gave similar results the Smagorinski was preferred, because the One Equation Eddy model was 1.5 times slower. That can be explained by the fact that One Equation Eddy model has one more equation to solve. In conclusion the Smagorinski model was chosen.

## Chapter 5

# Methodology

### 5.1 Geometry

The design of the geometries used in this thesis was based on the configuration that was proposed on THEMFE project meeting. The current simulation geometries covers the part of the total test section where the temperature fluctuations were to be expected.

In this thesis two separate geometries were considered. The detailed dimensions can be found in Appendices B and C. The difference between the first and the second case geometry can be seen in Figures B.1 and C.1. The positions of the cold flow (60°C) inlets are different. In the first case water was coming in through the annulus located at the bottom of the geometry, see cold inlet v1 marked in Figure 5.1. There were no inlets at the sides. In the second case there were inlets on the sides, but no inlet at the bottom annulus, see cold inlet v2 marked in Figure 5.1. The second case geometry is similar to the geometry that will be used in the THEMFE experiment. The purpose of having two different geometries was to see the effect of the cold flow on the flow in the mixing region. It was suspected to see cold jets in the mixing zone while using the second case geometry. In both cases the mass flow through the hot inlets was 0.8 kg/s and through the cold inlet(s) was 0.07 kg/s.

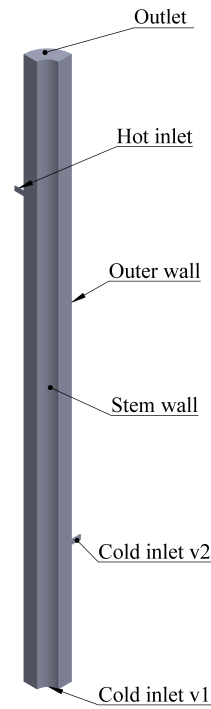


Figure 5.1: Quarter geometry. The simulations were done on full geometry.

## 5.2 Mesh

Two multi-block hexahedral grids were constructed. The advantage of using hexahedral cells over tetrahedral cells is that for the same cell count, hexahedral meshes will give a less diffusive solution compared to the one with tetrahedral cells, especially if the grid lines are aligned with the flow. Furthermore, hexahedral cells need more than two times less nodes to provide same physical resolution as in the case of tetrahedral mesh [4].

In multi-block grid generation, the geometry is first divided into smaller blocks which are thereafter separately meshed using structured mesh generation. A structured mesh is commonly built from hexahedrals by repeating its geometrical and topological structure [1].

In this thesis two different grids were constructed - one mesh per geometry. In both cases one quadrant of full geometry (Figures B.1 and C.1) was meshed and thereafter the mesh was mirrored twice to obtain the full mesh. The mirroring was first done in the plane x-y, then in the plane x-z. This approach was used to ensure that the mesh would be symmetric. Both grids contained only hexahedral cells and the total number of cells is presented in Table 5.1. The number of cells was picked to have enough refinement to ensure accurate results while being coarse enough to limit the required computing time. Courant-Friedrichs-Lewy condition [8][10]:

$$Co = \frac{v\Delta t}{\Delta x} \leq 0.5, \quad (5.1)$$

was used for optimizing the cell sizes  $\Delta x$  by knowing velocities  $v$  and by fixing time step value  $\Delta t$ . When  $Co \leq 1$  then the necessary condition for the solution stability is fulfilled [10].

Table 5.1: Mesh information

|                                       | Mesh 1  | Mesh 2  |
|---------------------------------------|---------|---------|
| Points                                | 1096456 | 1146256 |
| Faces                                 | 3155570 | 3298796 |
| Internal faces                        | 3022246 | 3159364 |
| Cells                                 | 1029636 | 1076360 |
| Boundary patches                      | 6       | 7       |
| Hexahedra                             | 1029636 | 1076360 |
| Max volume of cell (mm <sup>3</sup> ) | 8       | 8       |

When generating a mesh one has to specify the meshing parameters for different parts/surfaces. In both cases the maximum element size was defined to be 2 mm. The minimum element size was chosen globally to be 1 mm except for near the control rod stem wall (0.2 mm) and the expansion ratio was adjusted to 1.5. Refinement at the control rod stem wall (Figure D.2) was done in order to get more accurate results in the most interesting area - near the control rod stem. Additional refinement had to be done near the inlets (Figures D.4 and D.5) because otherwise the inlet flow would not have been accurate. Three factors were considered during meshing of the inlets: to have enough grid points on the grid surfaces perpendicular to flow direction (for having enough points to represent the velocity profile), to have the same cell size along the flow from the inlet to the stem wall, except near the stem wall where there is additional refinement described previously (to avoid sudden cell size changes in the flow direction) and to keep the mesh quality as high as possible.

Meshing had to be done in a way to reduce inaccuracies that might originate from the effect of local refinement: the flow can have an unphysical non-equilibrium state when it moves between regions with different cell sizes [10]. In other words we could expect to see abrupt changes in the LES solutions at the borders of the refinement regions. The meshing quality was improved by using O-Grid blocking to reduce the skewness where a block corner lies on a continuous curve or surface (Outer wall, Stem wall and outer walls of the inlets in Figure 5.1). It arranges the grid lines into an "O" shape. The most descriptive views of the resulting meshes can be seen in Appendix D.

One of the parameters that describe quality of the mesh is skewness. For hexahedral elements, skewness is defined as the normalized worst angle between each of the six faces normals and the vector defined by the centroid of the hexahedron and the center of the face, see Figure D.6 [16]. The skewness is normalized so that "1" denotes the ideal case and "0" the worst possible case. Both cases had skewness above 0.75 and most of the cells above 0.95 (Table 5.2).

Table 5.2: Mesh quality (skewness)

|                        | Mesh 1  | Mesh 2  |
|------------------------|---------|---------|
| 0.95 $\rightarrow$ 1   | 99.303% | 98.863% |
| 0.9 $\rightarrow$ 0.95 | 0.462%  | 0.692%  |
| 0.85 $\rightarrow$ 0.9 | 0.160%  | 0.285%  |
| 0.8 $\rightarrow$ 0.85 | 0.055%  | 0.117%  |
| 0.75 $\rightarrow$ 0.8 | 0.021%  | 0.043%  |
| 0 $\rightarrow$ 0.75   | 0%      | 0%      |

### 5.3 CFD Simulation

In this thesis all CFD simulations were carried out by using the free, open source (GNU General Public License) CFD toolbox called OpenFOAM (Open Field Operation and Manipulation) version 2.0.x. OpenFOAM is written in C++ programming language which is object-oriented and its overall structure can be seen in Figure 5.2. Its existing solvers can be modified or new ones can be created [13].

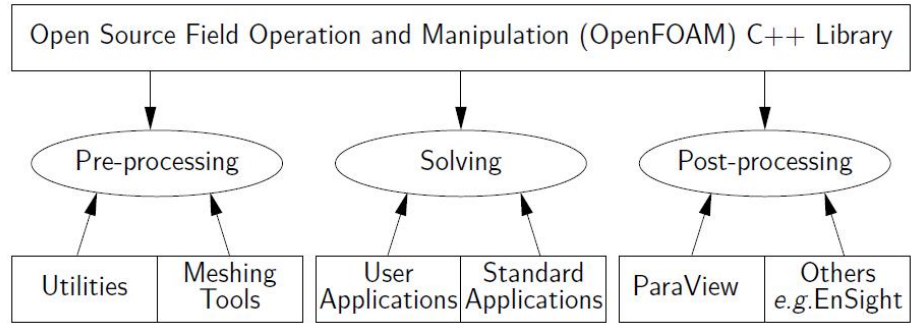


Figure 5.2: Overview of OpenFOAM structure [13]

The current work needs a transient solver that takes into account buoyancy effect, heat transfer, single-phase incompressible flow and uses an LES model. The solver that was used is called `buoyantBoussinesqGenPisoFoam` and it is based on OpenFOAM's standard solver `buoyantBoussinesqPisoFoam`. The reason for modifications was to add the LES capability. `BuoyantBoussinesqGenPisoFoam` was implemented by Nicolas Forsberg and Henrik Bergegrsen (both at Forsmark Kraftgrupp AB). Similar modifications are presented in [21].

For the RANS simulations the SIMPLE (Semi-Implicit Method for Pressure-Linked Equations) algorithm was used to create initial data for the transient simulation. For all transient simulations the PISO (Pressure Implicit with Splitting of Operators) algorithm was used. Both algorithms are explained in Table 5.3.



Table 5.3: SIMPLE and PISO algorithm [20, 22]

| SIMPLE algorithm   | PISO algorithm  |
|--|---|
| 1. Set the boundary conditions.<br>2. Solve the discretized momentum equation to compute the intermediate velocity field.<br>3. Compute the mass fluxes at the cells faces.<br>4. Solve the pressure equation and apply under-relaxation.<br>5. Correct the mass fluxes at the cell faces.<br>6. Correct the velocities on the basis of the new pressure field.<br>7. Update the boundary conditions.<br>8. Repeat till convergence. | 1. Set the boundary conditions.<br>2. Solve the discretized momentum equation to compute an intermediate velocity field.<br>3. Compute the mass fluxes at the cells faces.<br>4. Solve the pressure equation.<br>5. Correct the mass fluxes at the cell faces.<br>6. Correct the velocities on the basis of the new pressure field.<br>7. Update the boundary conditions.<br>8. Repeat from 3 for a prescribed number of times.<br>9. Increase the time step and repeat from 1. |

The problem to solve is specified in the case folder (boundary conditions, mesh, etc). The minimum set of required files needed for a case are shown in Figure 5.3 [13]. The case folder consists of three subfolders: system, constant and time directories (at the beginning there is only time directory "0").

During this thesis five different files were contained in the system folder: controlDict, fvSchemes, fvSolution, decomposeParDict and probesDescription. The file controlDict is used for setting up run control parameters (start/end time, time step) and parameters for data output. Usually probe description is included into controlDict, but in this thesis case separate file for probing locations was created. File fvSolution is used to set up equation solvers, tolerances and other algorithm

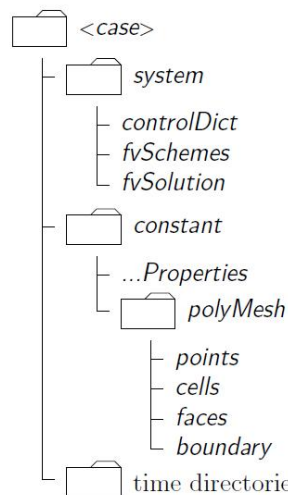


Figure 5.3: OpenFOAM case directories [13]

controls and in file fvSchemes discretization schemes are selected.

In constant folder one can find subfolder polyMesh that contains mesh and files: transportProperties, LESProperties, turbulenceProperties and g. File transportProperties contains specific physical properties, in turbulenceProperties turbulence model is selected, in g gravity direction is defined and in turbulenceProperties turbulence model and associated constants are defined.

Time directory folder "0" contains initial and boundary conditions for particular field that is demanded by solver. Thesis case "0" contains following files: k, nuSgs, p, T and U. The boundary conditions used are presented in Table 5.4.

Table 5.4: Boundary conditions

|             | Wall                       | Inlet                     | Outlet      |
|-------------|----------------------------|---------------------------|-------------|
| $k_{SGS}$   | kqRWallFunction            | fixedValue                | inletOutlet |
| $\nu_{SGS}$ | nuSgsUSpaldingWallFunction | calculated                | calculated  |
| p           | zeroGradient               | zeroGradient              | fixedValue  |
| T           | zeroGradient               | fixedValue                | inletOutlet |
| v           | fixedValue                 | radialProfile, fixedValue | inletOutlet |

- fixedValue- The fixed value boundary condition defines  $\Phi$  to have a value  $\Phi_b$  at the boundary  $b$  [17],
- zeroGradient- The normal gradient of  $\Phi$  at the boundary  $b$  is zero [10],
- inletOutlet- zeroGradient is applied to all faces on the boundary  $b$ , except for those where there is inflow, in which case fixedValue is used [13],
- calculated- Boundary field  $\Phi$  is calculated by using other fields [13],
- WallFunction- Empirical function for obtaining suitable conditions near the wall without having extremely refined grid,
- radialProfile- Radial profile boundary condition defines  $\Phi$  to have user specified radially symmetric profile at boundary  $b$ .

Boundary condition radialProfile was implemented by Nicolas Forsberg [12] and it was needed to define a radially symmetric velocity profile (Figures E.1 and E.2) for the inlets except for the annular cold inlet in the first geometry case, where fixed

value boundary condition was used. Velocity profiles were obtained by rescaling earlier measurement results done with different conditions [26]. Rescaling was done in a way to fit the velocity profile to the current geometry and to have the right mass flow. The obtained flow is not perfect but it simulated real conditions in a best possible way compared to a "flat" inlet velocity profile. The advantage of using a radial velocity profile boundary condition is that shorter inlets (15 mm, each containing 1314 cells) can be used to save mesh and computational time.

During the simulations second order discretization schemes and interpolations were used with different operators that can be seen in Table 5.5. Time derivative used implicit backward scheme. Other discretized operators used either Gauss or cell limited Gauss schemes. Interpolation was done by using a linear scheme with modifications that can be found in User Guide [13].

Table 5.5: Discretization and interpolation schemes

|                               | Discretization scheme | Interpolation scheme |
|-------------------------------|-----------------------|----------------------|
| $\frac{\partial}{\partial t}$ | backward              |                      |
| Gradient $\nabla$             | cellLimited Gauss     | linear               |
| Divergence $\nabla \cdot$     | Gauss                 | filteredLinear2V     |
|                               |                       | limitedLinear        |
|                               |                       | linear               |
| Laplacian $\Delta$            | Gauss                 | linear limited       |

Both simulation cases were set in a way to ensure that the maximum Courant number would stay in the range of 0.5. In that way the necessary condition for convergence was fulfilled. It was achieved by having a constant time step of 15  $\mu s$ . A constant time interval is important when Fourier Transformation is used on the results (discussed in the next subsection). Temperature and velocity data was sampled every 100 time steps. Probes were located on four vertical lines 1 mm outside the control rod stem shown in Figure 5.4. Positions "N" and "S" were aligned along the cold inlets and positions "W" and "E" were aligned along the hot inlets. Each probing line contained 225 probes that were equally spread along the line which passed the entire geometry.

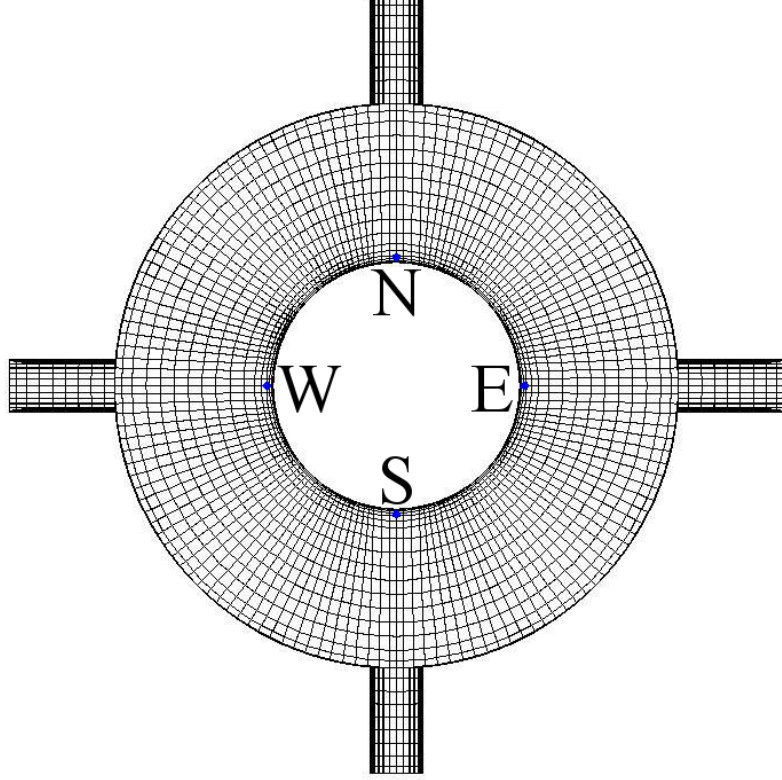


Figure 5.4: Probe locations (mesh viewed from above). The positions "W" and "E" were aligned along the hot inlets.

#### 5.4 Analysis of probed data

The data was analyzed using probes that extracted data at a set of points in space and time. The extracted probing data contained temperature  $T(\mathbf{x}, t_n)$ . Here " $n$ " denotes the number of the time step. For analyzing probe data the following parameters were calculated:

Mean temperature:

$$\bar{T}(\mathbf{x}) = \frac{1}{N} \sum_{n=1}^N T(\mathbf{x}, t_n). \quad (5.2)$$

Standard deviation of temperature ( $\sigma_T$ ) is defined as:

$$\sigma_T(\mathbf{x}) = \sqrt{\frac{1}{N} \sum_{n=1}^N (T(\mathbf{x}, t_n) - \bar{T}(\mathbf{x}))^2}. \quad (5.3)$$

Discrete Fourier Transformation ( $F_T$ ) of the temperature data:

$$F_T(\mathbf{x}, f_m) = \frac{T_t}{N} \sum_{n=1}^N (T(\mathbf{x}, t_n) - \bar{T}(\mathbf{x})) e^{-2\pi i m(n-1)/N}, \quad (5.4)$$

where  $m = 0, 1 \dots N-1$ ,  $i = \sqrt{-1}$ ,  $T_t$  is total measurement time. Mean temperature subtraction is done in order to eliminate the zero frequency in the Fourier spectrum which represents the mean value. In (5.4) following relationship holds:

$$f_m = m f_S, \quad (5.5)$$

where  $f_S$  is the sampling frequency. The temperature standard deviation in combination with the mean temperature can be used for determining the length of the mixing region. The largest temperature fluctuations are expected in the position where the standard deviation has its maximum value.

One of the main objectives of this master thesis, except from verifying that the proposed geometry would give rise to low frequent temperature oscillation, was to determine the frequency of these oscillations. Since low frequencies of the order of 0.1-1 Hz were expected, a relatively long simulation time was needed. 75 s of simulation data was obtained. It took approximately 2 months wall clock time while using 104 cores. In temperature Fourier spectrum "peaks" near 0.1 Hz were expected although 75 s only equals 7.5 full oscillations in that frequency range.

### Statistical convergence

The first five seconds of the data was not used to eliminate influence from initial conditions. Statistical convergence was estimated by studying relative mean temperature change:

$$\Delta \bar{T}(\mathbf{x}, t_n) = \frac{\bar{T}(\mathbf{x})_{t_n} - \bar{T}(\mathbf{x})_{t_{n-1}}}{\bar{T}(\mathbf{x})_{t_n}}. \quad (5.6)$$

Here subindex shows time steps that were included while calculating mean temperature. In equation (5.6) the mean temperature after every iteration was calculated and the relative change between two subsequent iterations was investigated. The data was considered to be statistically converged when  $|\Delta \bar{T}(\mathbf{x}, t_n)|$  was less than 0.01%. The statistical convergence was obtained after simulating the first 7 s (Figure 5.5) in the first case and 6.5 s (Figure 5.6) in the second case. Corresponding times in the most dangerous region, where the dominant high amplitude temperature oscillations have a frequency of the order of 0.1 Hz, were 6.2 s and 5.7 s.

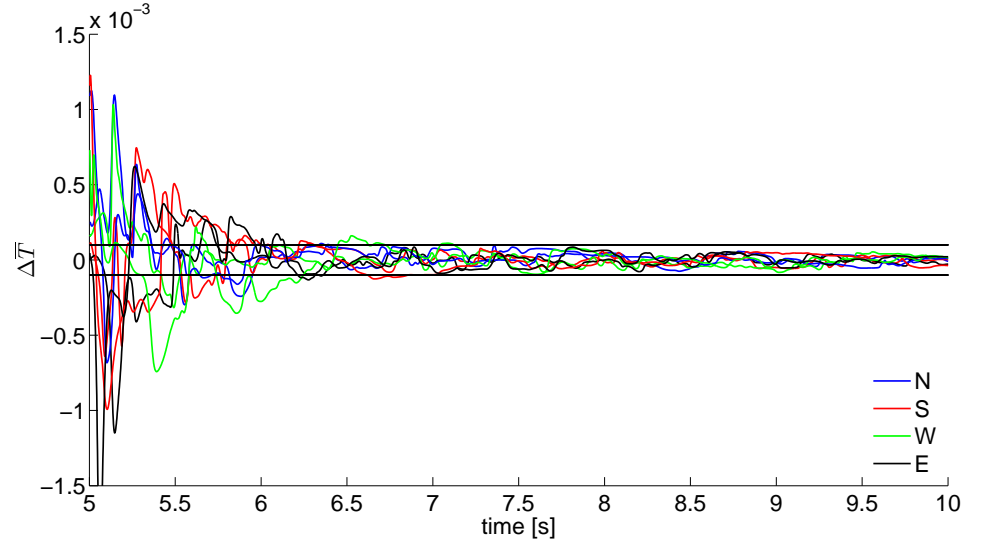


Figure 5.5: First case time series of the relative mean temperature change at the vertical position  $y = 0.45848$  m at the different probing locations.

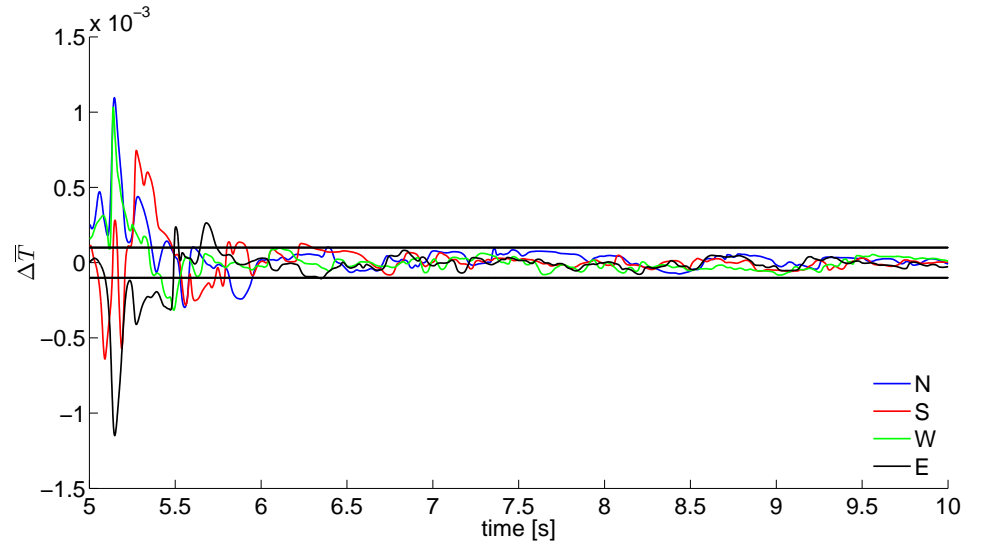


Figure 5.6: Second case time series of the relative mean temperature change at the vertical position  $y = 0.45848$  m at the different probing locations.

### Grid dependence

For studying the mesh size influence on the results two additional grids were constructed in the similar way as described before. The aim was to create meshes where the number of cells would be increased/decreased by two times compared to the mesh used in the first simulation case. Therefore factor  $\sqrt[3]{2}$  was used for obtaining the maximum and the minimum element lengths. The constructed grids were called "0.5 M" and "2 M" and the parameters compared with the grid used in the first case can be seen in Table 5.6. The grid "2 M" is prohibitively "expensive" to be used in the simulation even though it would give the most accurate results.

Table 5.6: Grid dependence study meshes

|                   | Hex. cells | Max el. size (mm) | Min el. size (mm) | Exp. ratio |
|-------------------|------------|-------------------|-------------------|------------|
| 0.5 M             | 533368     | 2.52              | 1.26 (0.25)       | 1.89       |
| First thesis case | 1029635    | 2                 | 1 (0.2)           | 1.5        |
| 2 M               | 2139184    | 1.59              | 0.8 (0.16)        | 1.3        |

The data from the first thesis case at the time step 30 s was mapped over new grids and 8.5 s of the simulation results were obtained. For the comparison mean temperatures 1 mm from the stem were calculated while using probe data from all four locations. The results can be seen in Figure 5.7.

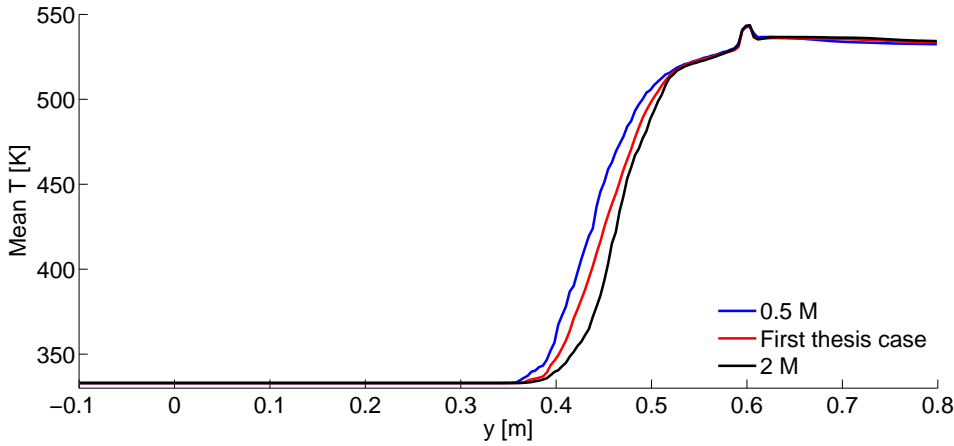


Figure 5.7: Mean temperature for different grids 1 mm from the stem wall.

One can observe that the mean temperatures differ mainly in the mixing region. It

appears that the coarser mesh "0.5 M" and the thesis case are over predicting the length of the mixing region. The difference when changing the grid size two times is below 32 K, see Figure 5.8. The usage of the first case grid is motivated by the fact that there is mean temperature difference below ten degrees in the region where the low frequent temperature oscillations occur ( $y \approx 0.39$  m), but most important, the "2 M" case would take 5 months of computing time and could not be afforded within this work.

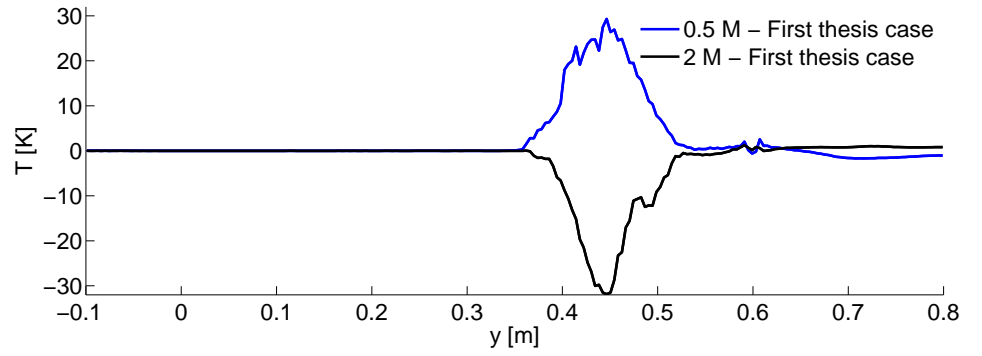


Figure 5.8: Over/under prediction compared with the thesis case.

Figure 5.9 shows that by improving mesh the mixing region length slightly decreases, the region moves vertically upwards and has a sharper "peak".

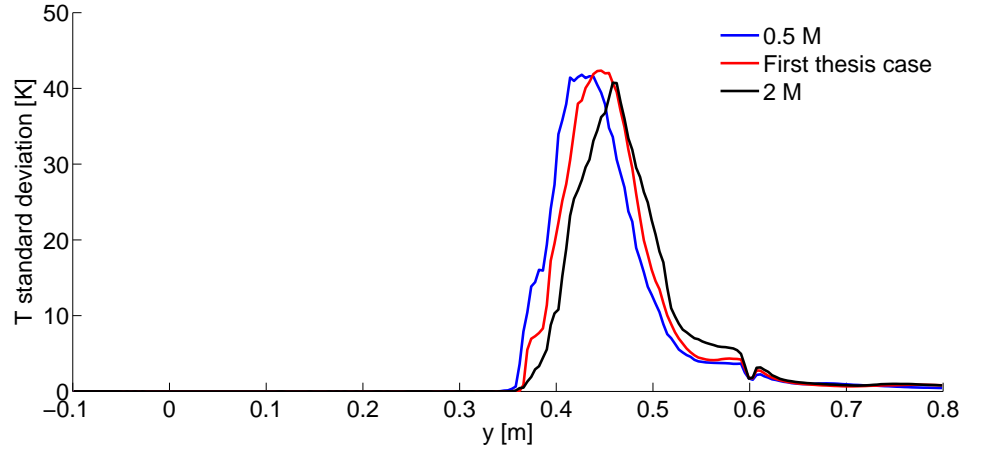


Figure 5.9: Temperature standard deviation for different grids 1 mm from the stem wall.



## 5.5 Flow through time

A rule of thumb usually used with LES is to start sampling after a time corresponding to 5-10 flow throughs. By assuming only the cold flow the residence time for the thesis case would be 51.5 s. Therefore to fulfill the rule of thumb, 257.5-515 s of the simulation time should be neglected. This would be prohibitively expensive. Therefore another approach would have to be used.

The time it takes for the hot flow to reach the vertically lower border of the mixing region was calculated. That time was doubled and the first 5 s in the data was neglected. That was the compromise used in order to get enough data for the thesis.



## Chapter 6

# Results and Discussion

In this part of the thesis, the results from the both cases are presented. In addition a short discussion concerning possible errors is given.

### 6.1 First case, with the cold flow coming from below

In Figure 6.1 the time series of the temperature 1 mm from the control rod stem at different vertical positions at the probing location "N" are shown. To get a better understanding of the vertical positions it should be noted that the position of the hot inlets is at  $y = 0.6$  m. The non-dimensional temperature, see equation (2.1), was used for displaying the results. One can observe a similar temperature behavior that was seen in the experiment carried out at Vattenfall Research & Development AB [2]. The overall mean temperature increases gradually upwards in the annular gap [2]. The maximum amplitude of the fluctuation, corresponds to  $T^*$  varying from 0 to 0.8, and it was observed at the vertical position  $y = 0.45848$  m. The position corresponds to the location where the standard deviation of  $T^*$  has its maximum value, see Figure 6.4. The low frequent temperature oscillation of the order of 0.1 Hz can be most clearly observed at the position  $y = 0.39018$  m. Low frequent oscillations of large amplitude are especially dangerous when it comes to thermal loads [2].

In Figure 6.2 the time series of temperature at different probing locations at the same vertical level are shown. It can be observed that the instantaneous flow is asymmetric. It should be noted that "heat bullets" can mainly be found at the positions "N" and "S". Applying a Fourier Transformation on the data from Figure 6.2, the temperature Fourier spectrum is obtained, see Figure 6.5. One can see that the Fourier spectrum has its high amplitude "peaks" below 0.6 Hz. Distinctive "peaks" can be found at positions "N" and "S" and the most dominant are around 0.1 Hz. The "peak" near 0.01 Hz can be excluded because simulation time was less than one full oscillation with that frequency.

In Figures 6.3 and 6.4 the mean temperature and its standard deviation can be seen at different probing locations as a function of the vertical position. In both figures the cold and the hot inlet locations are denoted as "CI" and "HI". The length of the mixing region can be estimated as  $y_{mix1} = [0.350; 0.550]$  m. The estimation is done by studying the temperature standard deviation. In the mixing region the positions "N" and "S" have slightly higher mean temperature and lower standard deviation compared to the positions "W" and "E". The mean temperature peak at "HI" for the positions "N" and "S" can be explained by the hot inlet jets hitting the stem wall at that position. The standard deviation stays below 50 K and it is 23% of the temperature difference between the hot and the cold inlet. The increase in temperature is most rapid in the first 15 cm of the mixing region, see Figure 6.13.

In the mixing region a flow in the circumferential direction was observed, see Figure 6.7. As a "heat bullet" penetrates into the colder flow with opposite direction it starts to rotate with an angular velocity of the order of  $\frac{\pi}{2} \frac{rad}{s}$ .

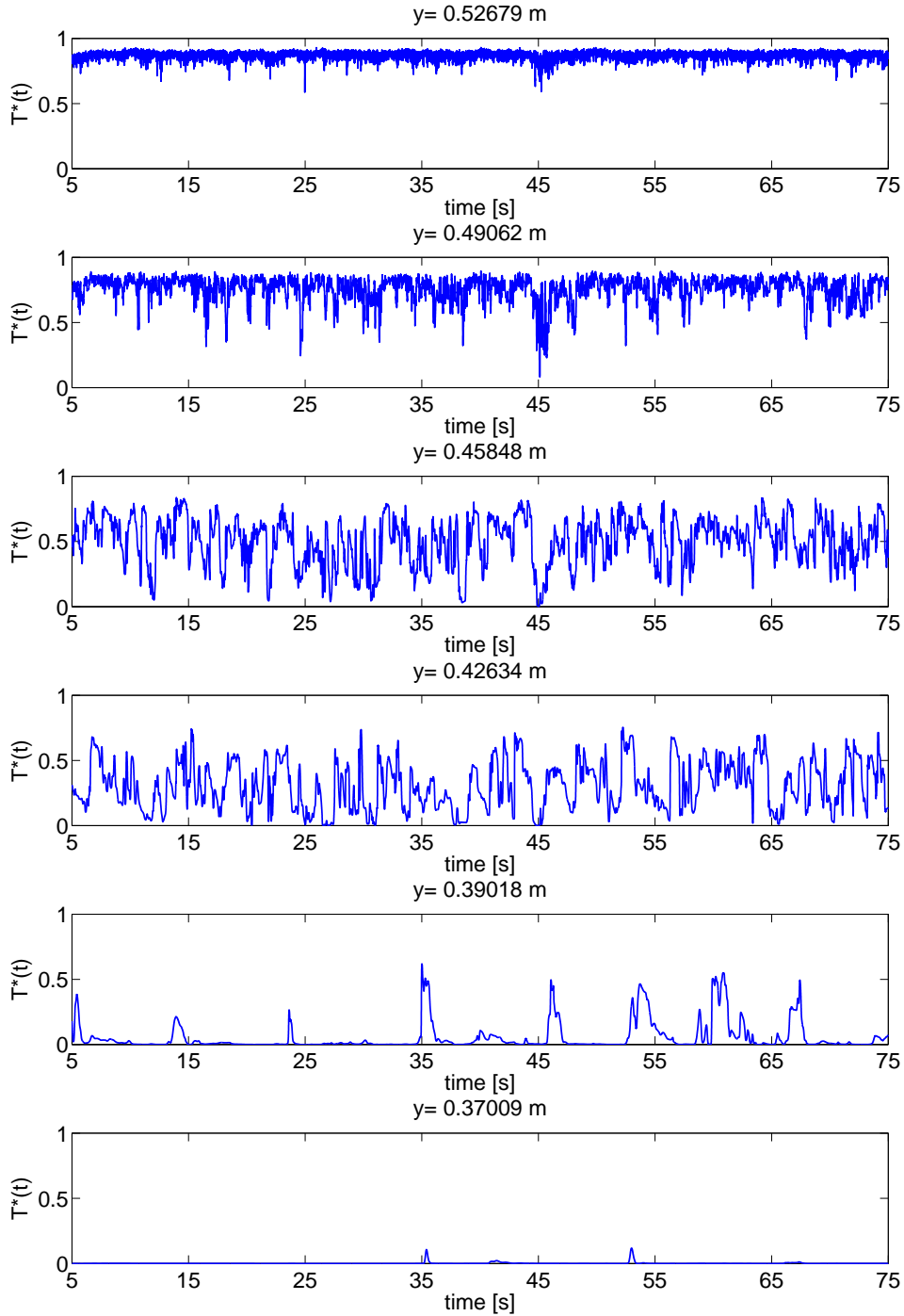


Figure 6.1: First case time series of the temperature 1 mm from the control rod stem at the different vertical positions at the probing location "N". The hot inlets are located at  $y = 0.6$  m.

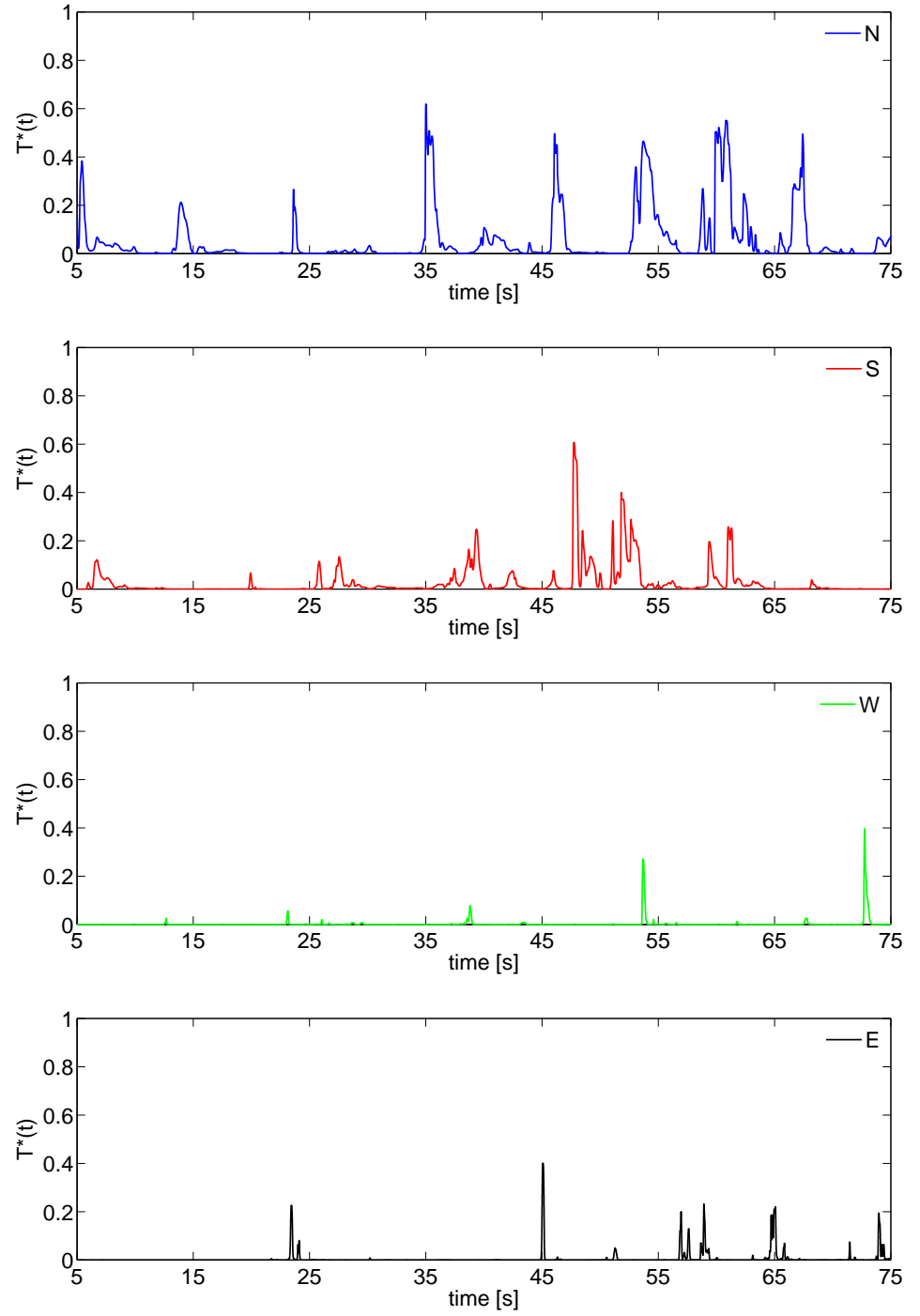


Figure 6.2: First case time series of the temperature at the vertical position  $y=0.39018$  m at the different probing locations.

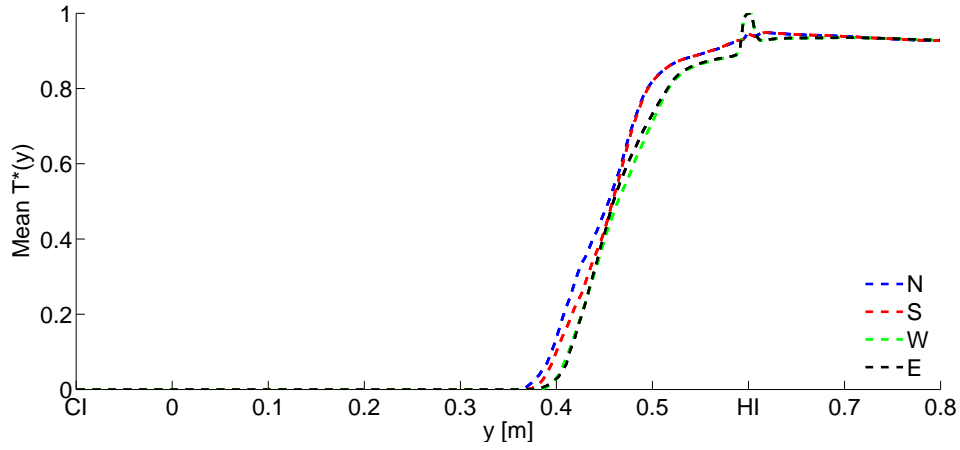


Figure 6.3: First case mean temperature at the different probing locations.

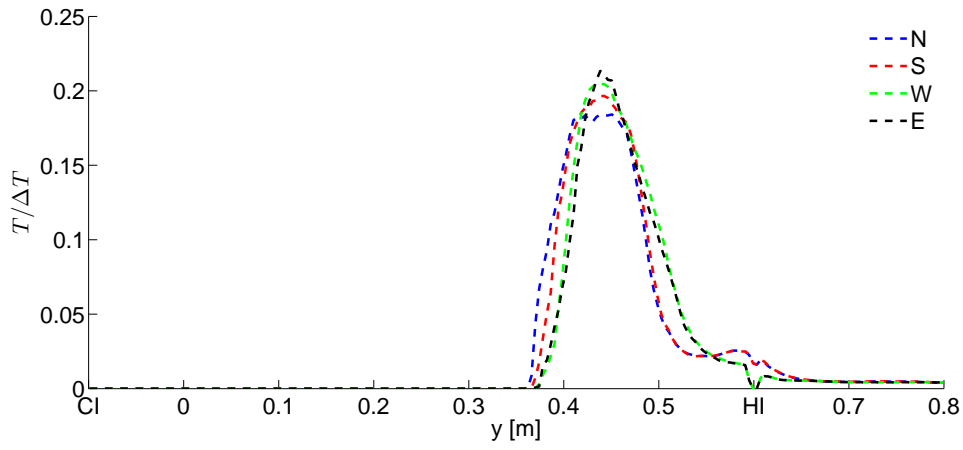


Figure 6.4: First case normalized temperature standard deviation at the different probing locations ( $\Delta T = 216$  °C).

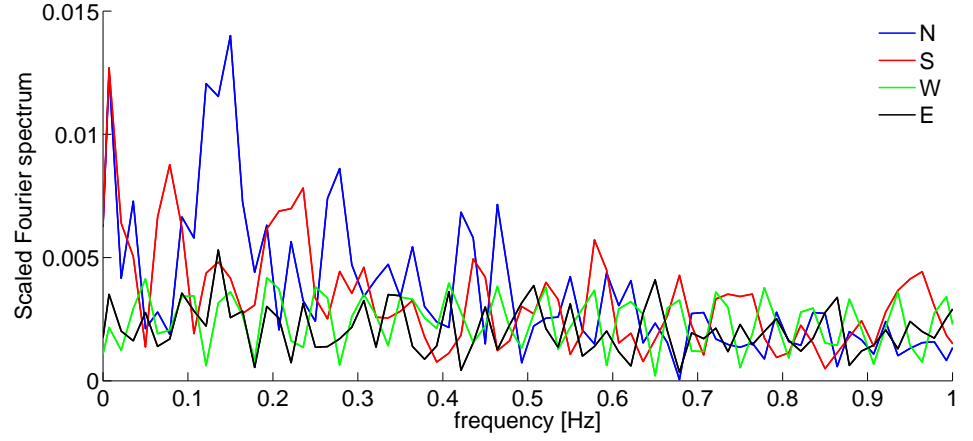


Figure 6.5: First case temperature Fourier spectrum at the vertical position  $y = 0.39018$  m at the different probing locations.

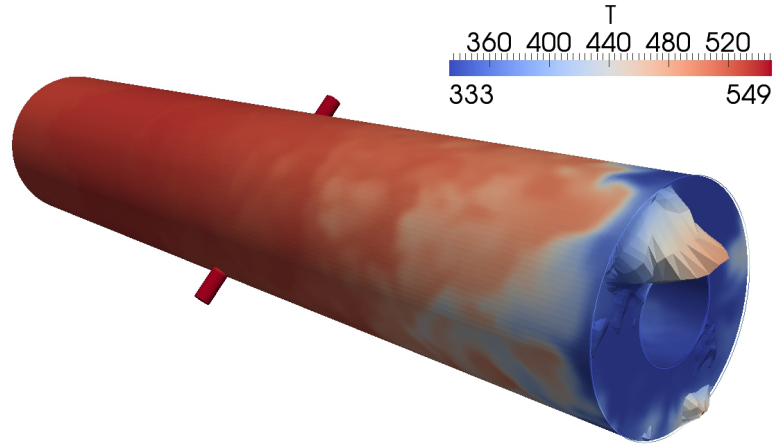


Figure 6.6: "Heat bullet" at the vertical positions  $y = 0.39018$  m at the simulation time  $t = 34.8$  s. First case geometry is shown at the interval  $y = [0.39018; 0.8]$  m. "Heat bullet" is visualized by making wrapped slice of velocity at the vertical position  $y = 0.39018$  m, which is colored by the temperature.



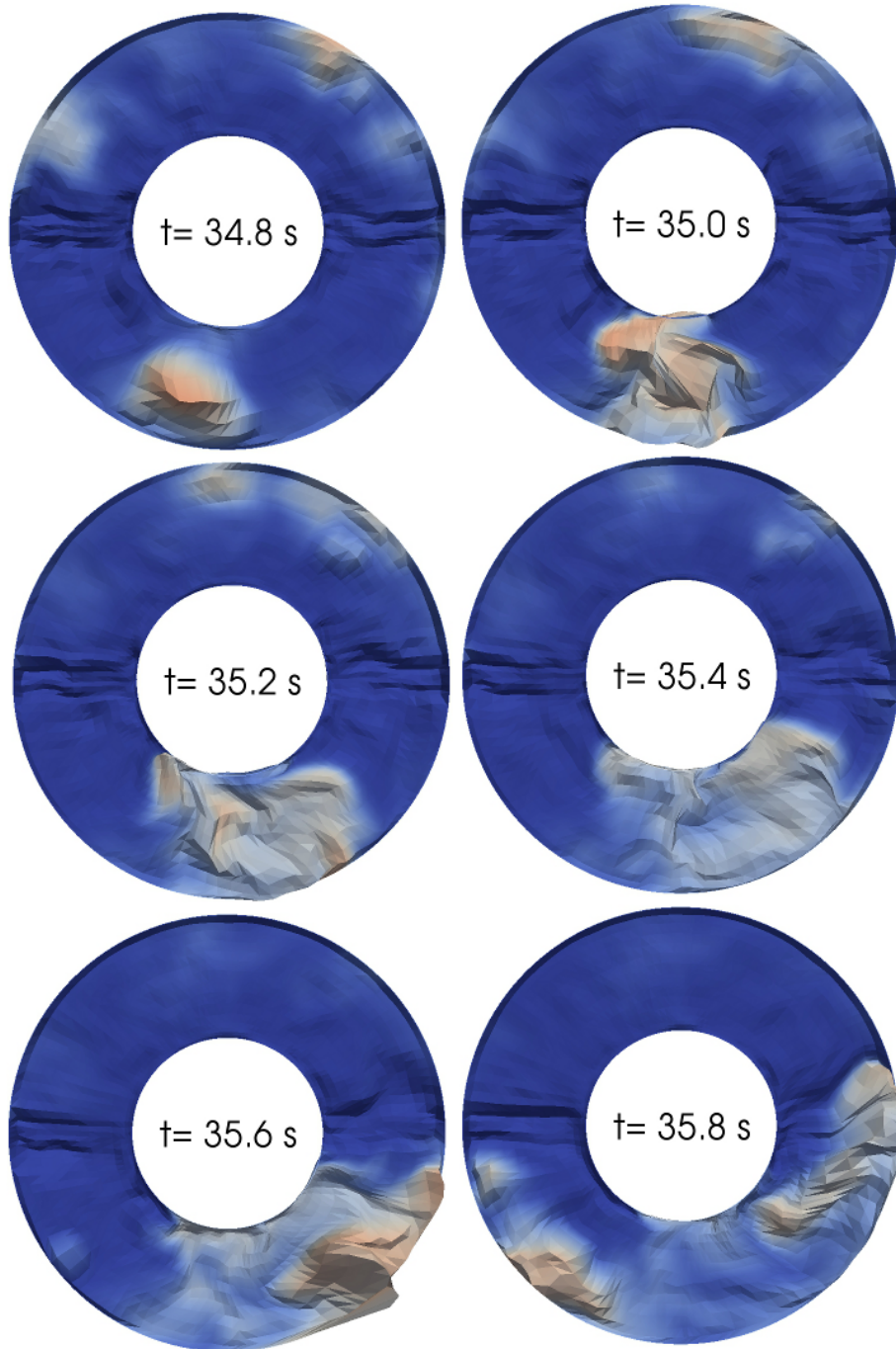


Figure 6.7: The time series of the flow movement in the annulus at the vertical positions  $y = 0.39018 \text{ m}$ . "Heat bullet" counterclockwise movement seen from below. The pictures are showing wrapped slices of velocity colored by the temperature.

## 6.2 Second case, with the cold inlets from the sides

The second geometry used differs only by the location of the cold inlet(s), see Figure 6.13. The aim was to see if the cold inlets from the sides would influence the results. It was suspected to see cold jets in the mixing zone while using second geometry (Figure C.1). If cold jets were to be seen then one of the possible solutions to eliminate their effect in the experiment would be to use a perforated plate to even out the flow from the jets in the annular gap.

By comparing Figures 6.2 and 6.8 one can notice that there are considerably more "peaks" from the probe locations "W" and "E" when using the second geometry. These extra "peaks" are indirectly caused by the cold jets. While "heat bullets" are penetrating vertically downwards at the positions "N" and "S", cold jets are moving vertically upwards at the positions "W" and "E". Due to these movements flow rotation perpendicular to vertical direction increases. Rotation of the "heat bullets" causes temperature "peaks" at the positions "W" and "E".

Figures 6.4, 6.10, 6.12 and 6.13 show that the mixing region  $y_{mix2} = [0.325; 0.550]$  m is 2.5 cm longer compared to the first case. The same tendency can be seen by comparing the mean temperatures, see Figures 6.3 and 6.9.

In Figure 6.11 one can see that Fourier spectrum has its high amplitude "peaks" again below 0.6 Hz, but this time most dominant "peaks" are located at the positions "W" and "E".

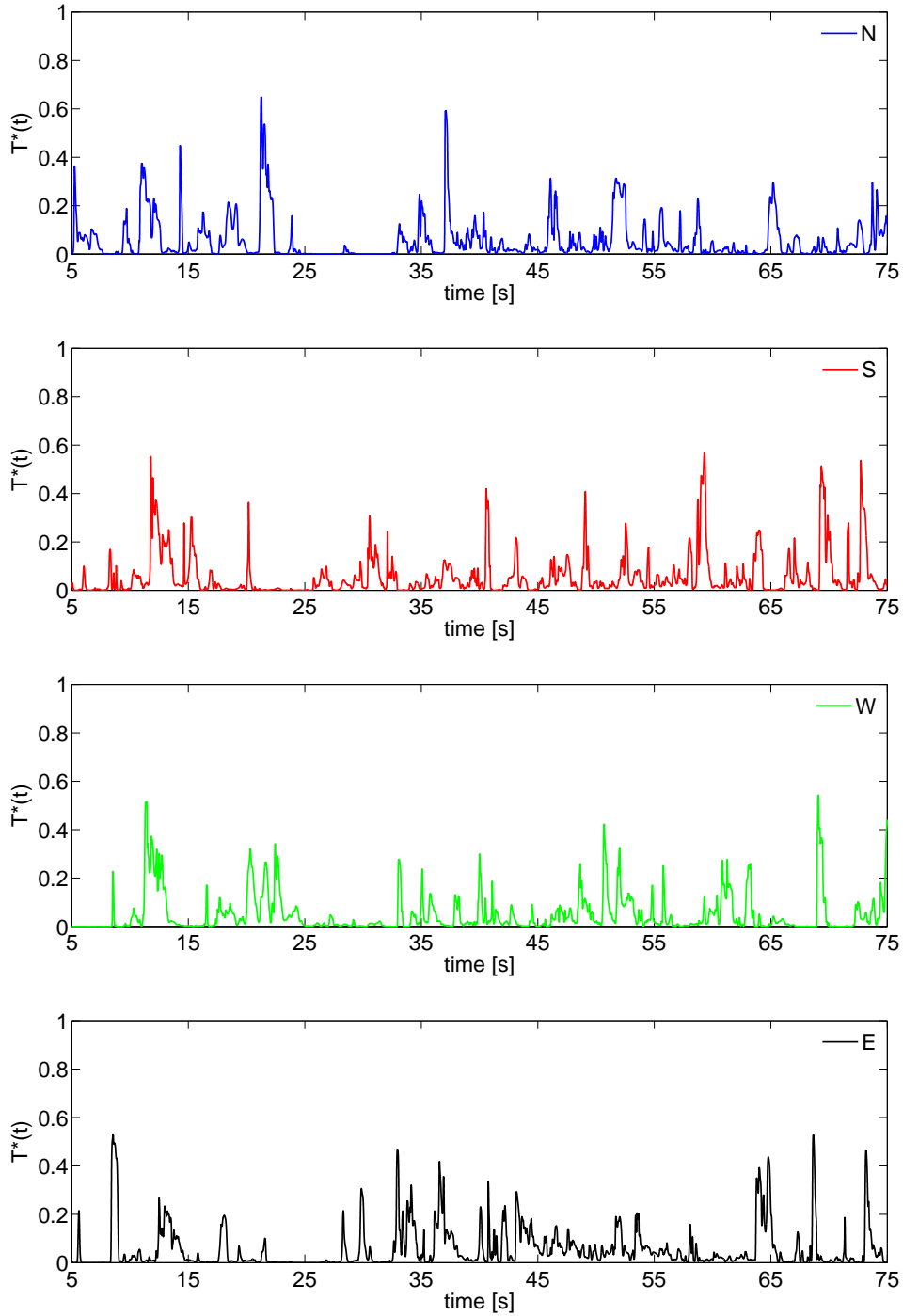


Figure 6.8: Second case time series of the temperature at the vertical position  $y=0.39018$  m at the different probing locations.

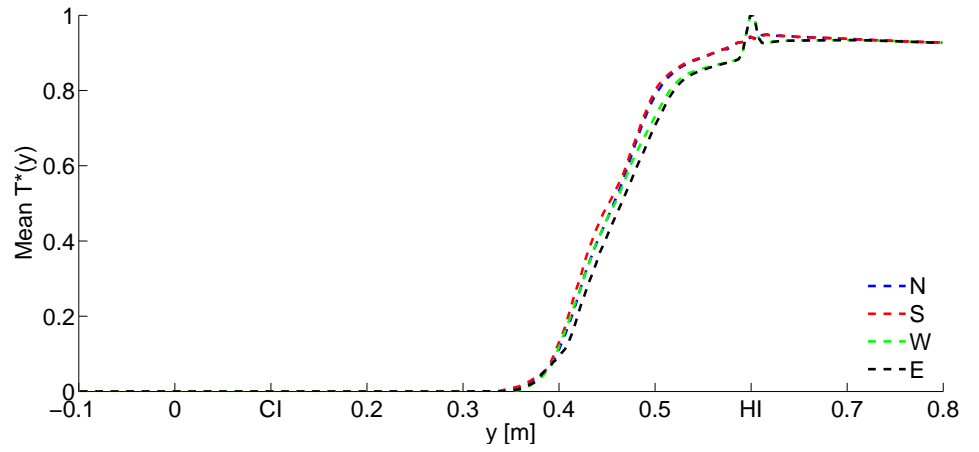


Figure 6.9: Second case mean temperature at the different probing locations.

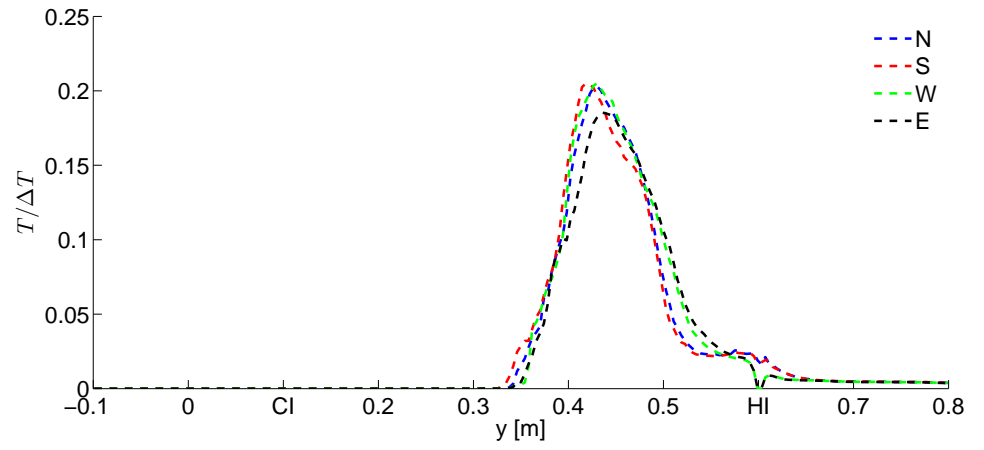


Figure 6.10: Second case normalized temperature standard deviation at the different probing locations ( $\Delta T = 216$  °C).

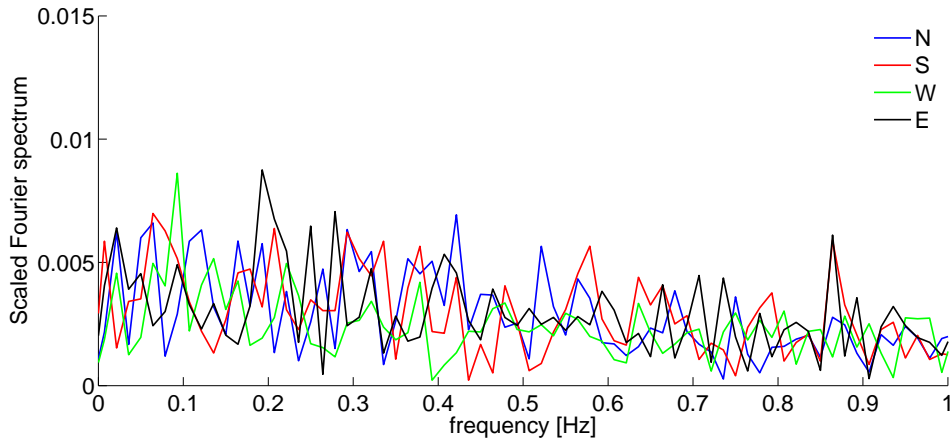


Figure 6.11: Second case temperature Fourier spectrum at the vertical position  $y = 0.39018$  m at the different probing locations.

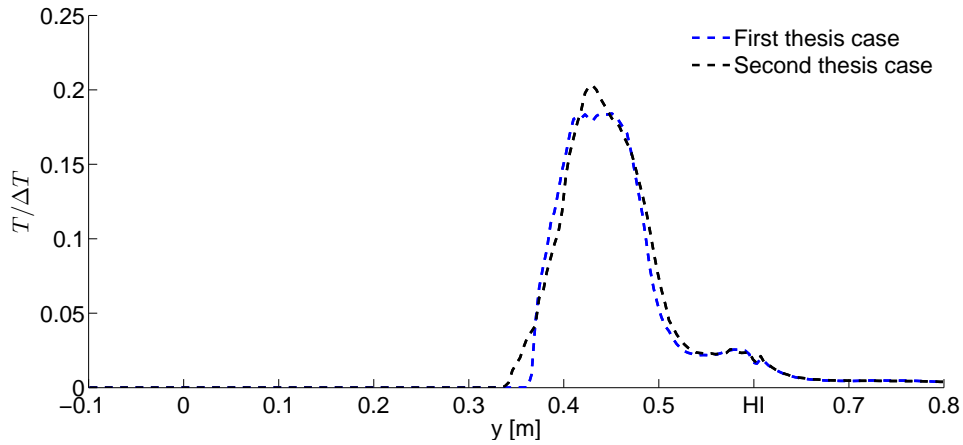


Figure 6.12: Normalized temperature standard deviation comparison at the probing location "N" ( $\Delta T = 216$  °C).

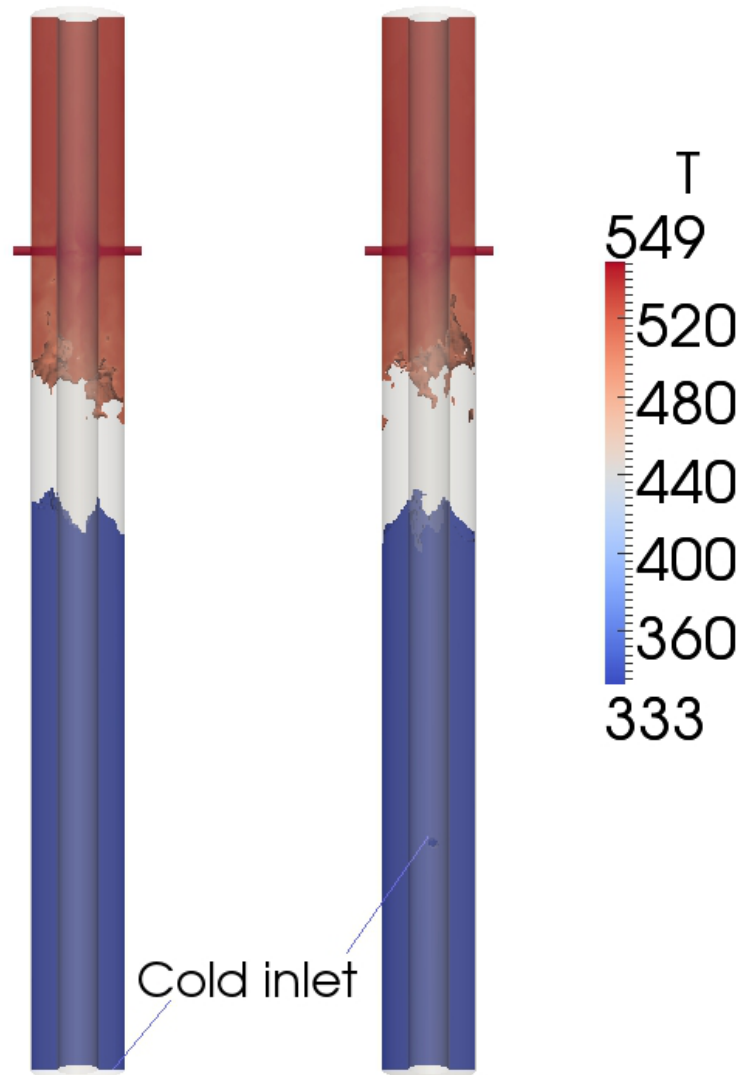


Figure 6.13: Visualization of the region where the temperature increases rapidly from 333 to 520 K. (Cut view from symmetry plane).

### 6.3 The most dangerous region

The length of the mixing region where the most dominant "peaks" in the temperature Fourier spectrum lie near the 0.1 Hz had to be estimated, because the low frequent oscillations of large amplitude are especially dangerous when it comes to thermal loads [2]. The estimation was done by investigating the temperature oscillation amplitude and its Fourier spectrum. The purpose was to find the region where the scaled Fourier spectrum has a value over 0.007 near the frequency of 0.1 Hz and the amplitude is larger than 50 K.

The most dangerous region for the first case was  $y_{d1} = [0.374; 0.406]$  m and for the second case  $y_{d2} = [0.370; 0.402]$  m. These regions have the same length and are shifted by 4 mm. The most dangerous region is less than 4 cm long and it would be advisable to use this information when planning the locations of the sensors for the experiment.

### 6.4 Constant transport properties

The model that was used in the simulations assumes that the transport properties are constant. The transport properties are density ( $\rho$ ), molecular kinematic viscosity ( $\nu$ ), thermal conductivity ( $\lambda$ ) and specific heat capacity ( $c_p$ ). This assumption might be a source of error that is estimated in the following section. The constant transport properties are compared with the conditions of  $T = 60$  °C and  $T = 276$  °C. The pressure change is small within the test section, hence their dependence of local pressure changes are neglected.

The constant values used in the simulations were obtained from the IAPWS IF-97 steam tables with conditions of  $p = 70$  bar and  $T = 200$  °C. The physical properties at different temperatures can be seen in Table 6.1. The largest difference is observed with the molecular kinematic viscosities, where the ratio of the viscosity at 60 °C and 200 °C is  $\approx 200$  %. The ratio of other properties is below 16 %.

In eddy viscosity models the effective kinematic viscosity,  $\nu_{eff} = \nu + \nu_{t/SGS}$ , is used. If the  $\nu_{t/SGS}$  is at least an order of magnitude larger than the  $\nu$ , then the first is dominating in the effective kinematic viscosity and the exact value of the  $\nu$  can be approximated by constant value over the whole temperature interval.

Above the mixing region  $\nu_{SGS}$  had values above  $1.3 \cdot 10^{-6} \text{ m}^2/\text{s}$ , except for a few spots near the the walls. The effective kinematic viscosity is dominantly dependent on  $\nu_{SGS}$  in this region and the effective kinematic viscosity is overestimated by 2 % of its value at the most.

Below the mixing region  $\nu_{SGS}$  had values above  $0.4 \cdot 10^{-6} \text{ m}^2/\text{s}$ . In this region the

effective kinematic viscosity is underestimated by  $\frac{1}{3}$  of its value at the most. The under/overestimation in the mixing region lies between these two cases discussed and depends on the temperature.

The Reynolds and Richardson numbers for the cold flow in the annulus are  $Re = 1655$  and  $Ri = 740$ . A physical interpretation of the  $Re$  is the ratio of the inertial versus the viscous forces. The  $Ri$  is the ratio of the the potential to the kinetic energy. Since  $Ri \gg 7$ , buoyancy effects are greater than inertial effects, at least far away from the jets. Since gravitational effects are more important than inertial effects and inertial effects are more important than viscous ones, errors due to wrong physical viscosity should be small. However this might not be true in the near wall region. Hence for future CFD validation work, it is recommended that the models with non constant viscosity are used.

The results presented in this work could have been improved by using models that use the steam tables. However steam tables are computationally very expensive. Hence a model that uses polynomial expression for  $\nu = \nu(T)$  is recommended.

Table 6.1: Water properties

|                                   | 70 bar, 200°C        | 70 bar, 60°C         | 70 bar, 276°C        |
|-----------------------------------|----------------------|----------------------|----------------------|
| $\rho [kg/m^3]$                   | 867                  | 986                  | 759                  |
| $\nu [m^2/s]$                     | $1.56 \cdot 10^{-7}$ | $4.75 \cdot 10^{-7}$ | $1.28 \cdot 10^{-7}$ |
| $\lambda [J/(m \cdot s \cdot K)]$ | 0.668                | 0.654                | 0.585                |
| $c_p [J/(kg \cdot K)]$            | 4463                 | 4168                 | 5191                 |



## Chapter 7

# Conclusions

The most important conclusions of this thesis are the following:

- It was verified that the proposed geometry and flow conditions for the THEMFE experiment give rise to the expected flow field. The simulations revealed that both considered geometries will generate low frequent temperature oscillations of the order of 0.1-1 Hz in the mixing region. Enough data has been obtained to conclude that the patterns exist.
- The results of this thesis indicate that the length of the mixing region is 23 cm. This is similar to the earlier experiment [2] and is large enough to be resolved in the THEMFE experiment.
- It was also found that the most dangerous region, where the dominant high amplitude temperature oscillations have a frequency of the order of 0.1 Hz, is 4 cm long. It would be advisable to use this information when planning the locations of the sensors for the experiment.
- It would be best to use a perforated plate in the THEMFE experiment to even out the cold flow. In that case results similar to the first CFD case will be expected, which show more clearly low frequent nature of the mixing region.
- It can be observed that the instantaneous flow is asymmetric. Therefore it is not recommended to use only a quarter of the geometry, neither in CFD nor in the experiments, because with a quarter geometry the effect of rotating flow in the circumferential direction cannot be captured.
- The results of this thesis support the idea that the cold inlets cannot be approximated as "flat" inlet, based on the differences observed between the two thesis cases.

- This study could be improved by using models that make use of steam tables, in order to take the variation of the density and viscosity with temperature into account. The effect is believed to be rather small to affect the overall conclusions in the thesis.
- A notable difference between the finer 2 M cell case and the presented case was observed. It is therefore recommended that smaller cell sizes are used for future CFD validation work. A grid size convergence test is highly recommended.

# Bibliography

- [1] Sudarsan N.S Acharya. A general survey of hexahedral mesh generation. [http://www10.informatik.uni-erlangen.de/~pflaum/pflaum/SeminarGrid\\_04/Refs/seminar.pdf](http://www10.informatik.uni-erlangen.de/~pflaum/pflaum/SeminarGrid_04/Refs/seminar.pdf), July 2004. Accessed 13 April 2012.
- [2] Kristian Angele, Ylva Odemark, Mathias Cehlin, Bengt Hemström, Carl-Maikel Högström, Mats Henriksson, Hernan Tinoco, and Hans Lindqvist. Flow mixing inside a control-rod guide tube- Experimental tests and CFD simulations. *Nuclear Engineering and Design*, 241:4803–4812, 2011.
- [3] Henryk Anglart. Thermal Hydraulics in Nuclear Systems. Nuclear Reactor Technology Division, Royal Institute of Technology (KTH), Stockholm, Sweden, 2010.
- [4] Andre Bakker. Information on Computational Fluid Dynamics, Lecture 7- Meshing. <http://www.bakker.org/dartmouth06/engs150/>. Accessed 13 April 2012.
- [5] Pierre-Antoine Bois. Joseph Boussinesq (1842-1929): A Pioneer of Mechanical Modelling at the End of the 19th Century. *Comptes Rendus MEcanique*, 335(9-10):479–495, October 2007.
- [6] Alexandre Chatelain, Frederic Ducros, and Olivier Metais. LES of turbulent heat transfer: proper convection numerical schemes for temperature transport. *International Journal for Numerical Methods in Fluids*, 44(9):1017–1044, March 2004.
- [7] United States Nuclear Regulatory Commission. Information on Control Rod Cracking Found at Swedish BWRs. <http://pbadupws.nrc.gov/docs/ML0833/ML083330227.html>, December 2008. Accessed 5 February 2012.
- [8] Richard Courant, Kurt Friedrichs, and Hans Lewy. Über die partiellen Differenzengleichungen der mathematischen Physik. *Mathematische Annalen*, 100(1):32–74, 1928.
- [9] Lars Davidson. Fluid mechanics, turulent flow and turbulence modeling. <http://www.tfd.chalmers.se/~lada>, Chalmers University of Technology, Goteborg, Sweden, November 2011.

- [10] Eugene de Villiers. *The Potential of Large Eddy Simulation for the Modeling of Wall Bounded Flows*. PhD dissertation, Imperial College of Science, Technology and Medicine, Department of Mechanical Engineering, July 2006.
- [11] Nicolas Forsberg. Simulation of Acoustic Waves in a Turbo-Fan Engine Air Intake. Master thesis, Uppsala Universitet, Teknisk- naturvetenskaplig fakultet, March 2009.
- [12] Nicolas Forsberg. radialProfile. Private communications, 2012.
- [13] OpenFOAM Foundation. OpenFOAM User Guide. <http://www.openfoam.org/docs/>, December 2011. Accessed 15 April 2012.
- [14] Yejun Gong and Franz X. Tanner. Comparison of RANS and LES Models in the Laminar Limit for a Flow Over a Backward- Facing Step Using OpenFOAM. Conference paper, Nineteenth International Multidimensional Engine Modeling Meeting at the SAE Congress, Detroit, Michigan, USA, April 2009.
- [15] Donald D. Gray and Aldo Giorgini. The Validity of the Boussinesq Approximation for Liquids and Gases. *Int. J. Heat Mass Transfer*, 19:545–551, 1976.
- [16] ANSYS Inc. ICEM CFD Help Manual. <http://www1.ansys.com/customer/content/documentation/140/icemcfd/icmhelp.pdf>, November 2011. Accessed 17 April 2012.
- [17] Hrvoje Jasak. *Error Analysis and Estimation for the Finite Volume Method with Application to Fluid Flows*. PhD dissertation, University of London, Department of Mechanical Engineering, June 1996.
- [18] Yuan Ma. CFD Simulation of T-Junction. Master thesis, Royal Institute of Technology (KTH), Department of Physics, August 2010.
- [19] Edouard Michta. Modeling of Subcooled Nucleate Boiling with OpenFOAM. Master thesis, Royal Institute of Technology (KTH), Department of Physics, February 2011.
- [20] OpenFOAMWiki. The PISO algorithm in OpenFOAM. [http://openfoamwiki.net/index.php/The\\_PISO\\_algorithm\\_in\\_OpenFOAM](http://openfoamwiki.net/index.php/The_PISO_algorithm_in_OpenFOAM), November 2009. Accessed 14 April 2012.
- [21] OpenFOAMWiki. BuoyantBoussinesqPisoFoam. <http://openfoamwiki.net/index.php/BuoyantBoussinesqPisoFoam>, June 2010. Accessed 14 April 2012.
- [22] OpenFOAMWiki. The SIMPLE algorithm in OpenFOAM. [http://openfoamwiki.net/index.php/The\\_SIMPLE\\_algorithm\\_in\\_OpenFOAM](http://openfoamwiki.net/index.php/The_SIMPLE_algorithm_in_OpenFOAM), March 2010. Accessed 14 April 2012.

- [23] Henrik Rusche. *Computational Fluid Dynamics of Dispersed Two-Phase Flows at High Phase Fractions*. PhD dissertation, Imperial College of Science, Technology and Medicine, Department of Mechanical Engineering, December 2002.
- [24] Scott Stolpa. Turbulent heat transfer. <http://nd.edu/~msen/Teaching/ThConv/THT.pdf>, Department of Aerospace and Mechanical Engineering, University of Notre Dame, Notre Dame, USA, April 2004.
- [25] Herman Tinoco and Hans Lindqvist. Thermal Mixing Instability of the Flow Inside a Control-Rod Guide Tube. Conference paper N13P1245, The 13th International Topical Meeting on Nuclear Reactor Thermal Hydraulics (NURETH-13), Kanazawa City, Ishikawa Prefecture, Japan, September 2009.
- [26] Johan Westin, Pascal Veber, and Lars Andersson. High-Cycle Thermal Fatigue in Mixing Tees: Large-Eddy simulations Compared to a New Validation Experiment. Conference paper ICONE16-48731 pp. 515-525, 16th International Conference on Nuclear Engineering (ICONE16), Orlando, Florida, USA, May 2008.



## Appendix A

### Control rod

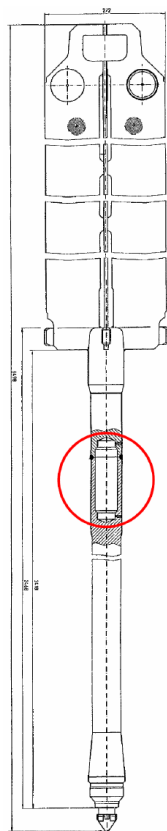


Figure A.1: Control rod with welded connection between blades and stem [25]





## Appendix B

### Geometry of the first case



Figure B.1: Isometric view of the first case geometry

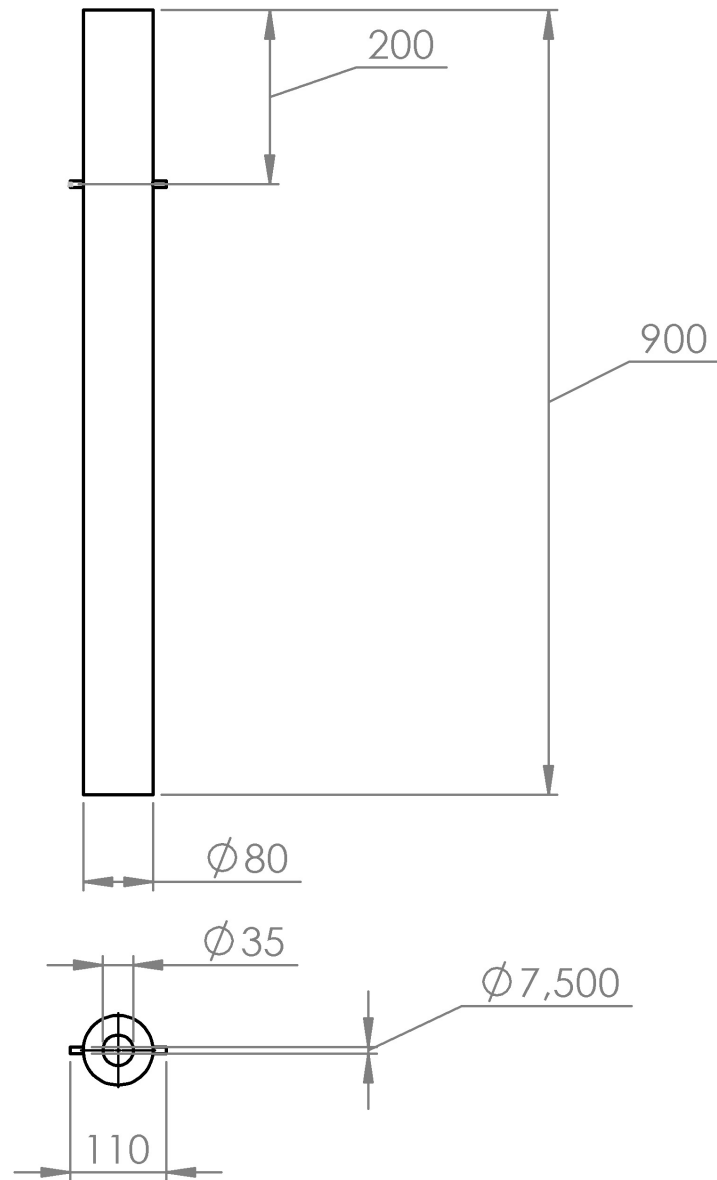


Figure B.2: Dimensions of the first case geometry

## Appendix C

### Geometry of the second case



Figure C.1: Isometric view of the second case geometry

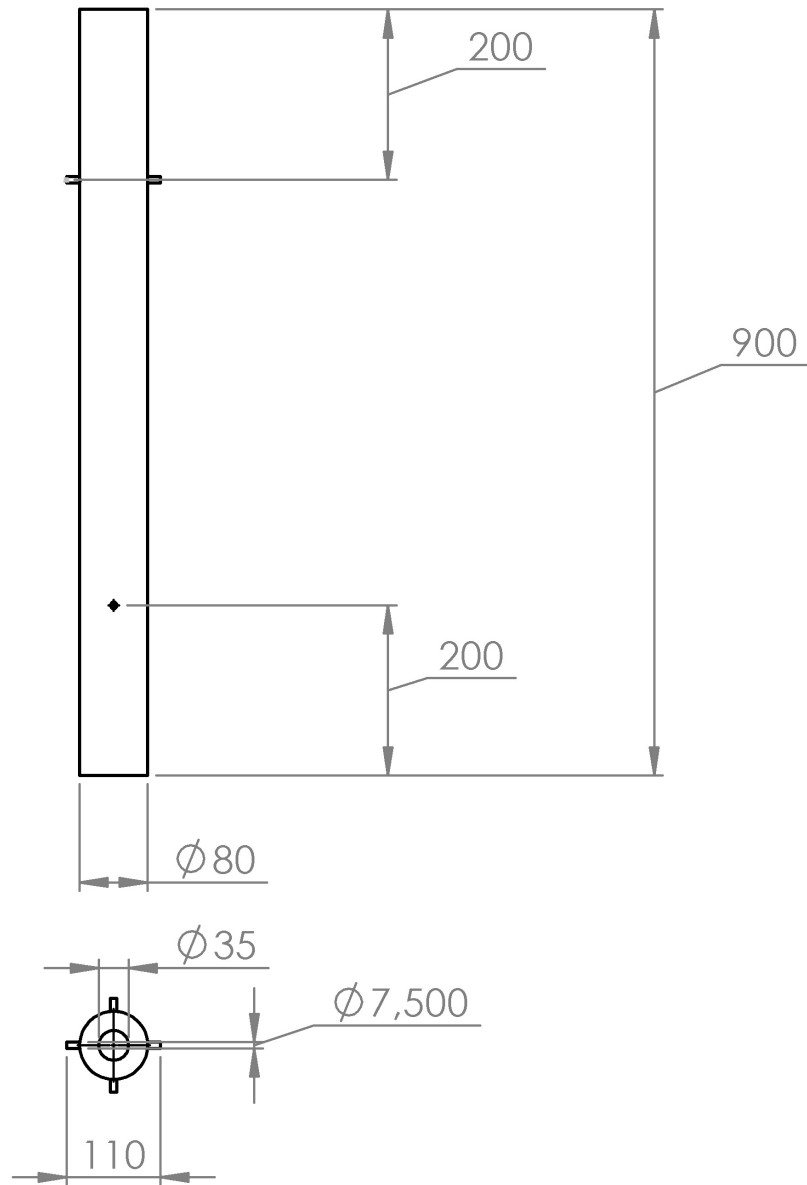


Figure C.2: Dimensions of the second case geometry

## Appendix D

### Mesh

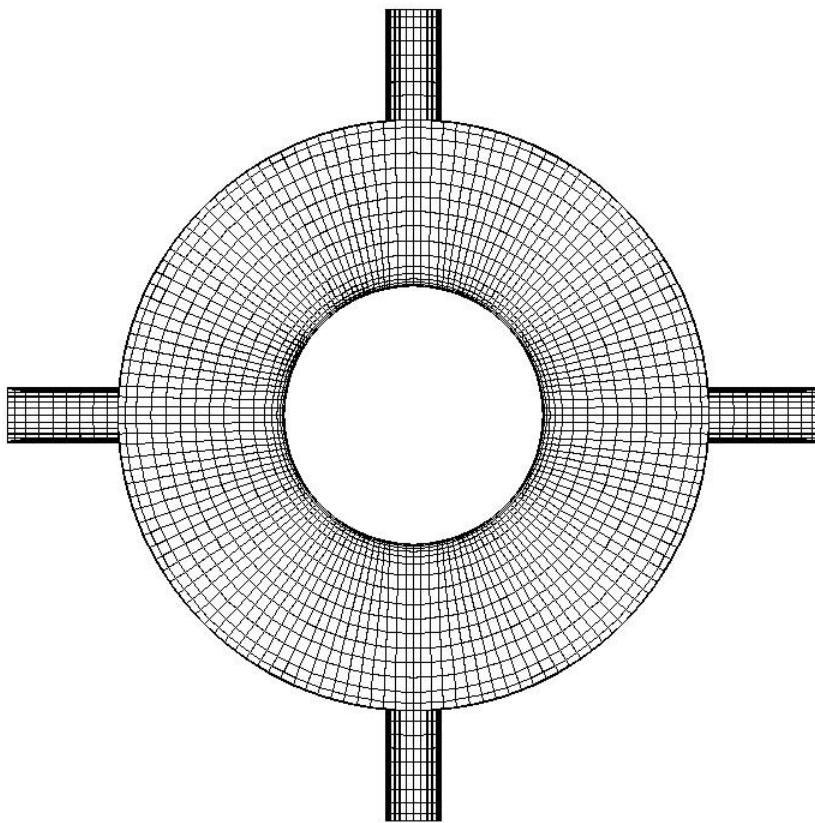


Figure D.1: Top view of the mesh

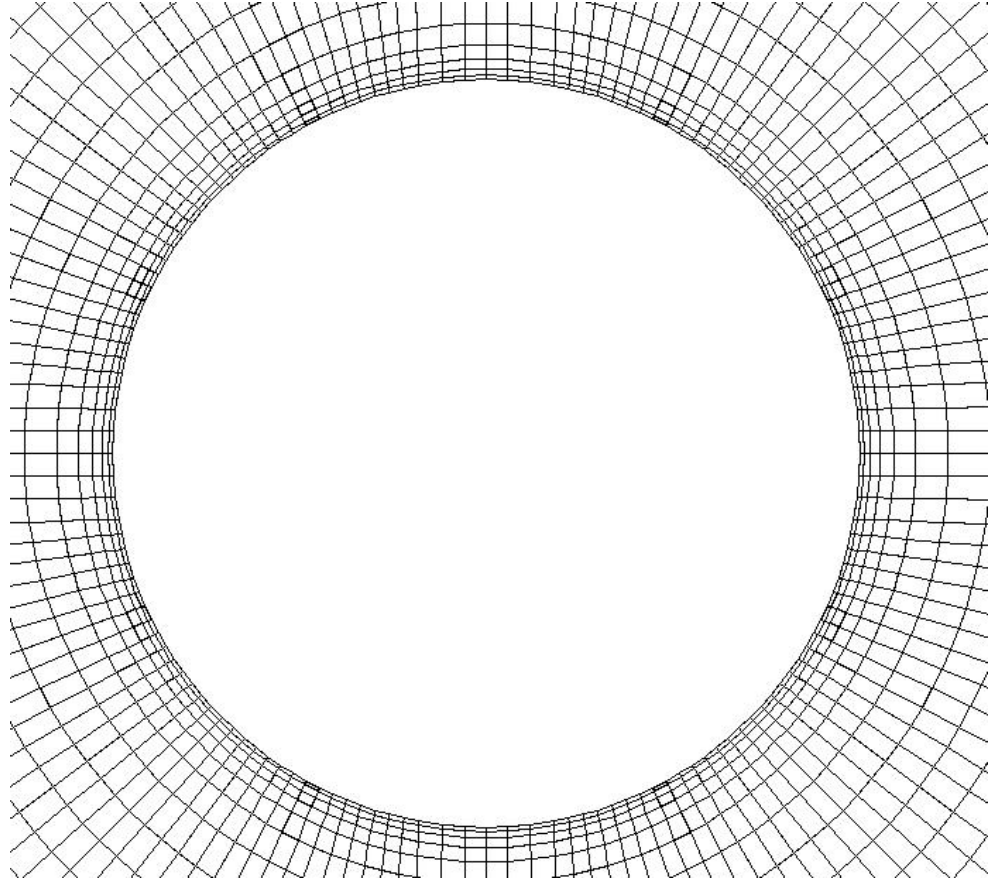


Figure D.2: Zoomed top view of the mesh (Mesh is refined near the stem wall to get more accurate results in the most interesting area)

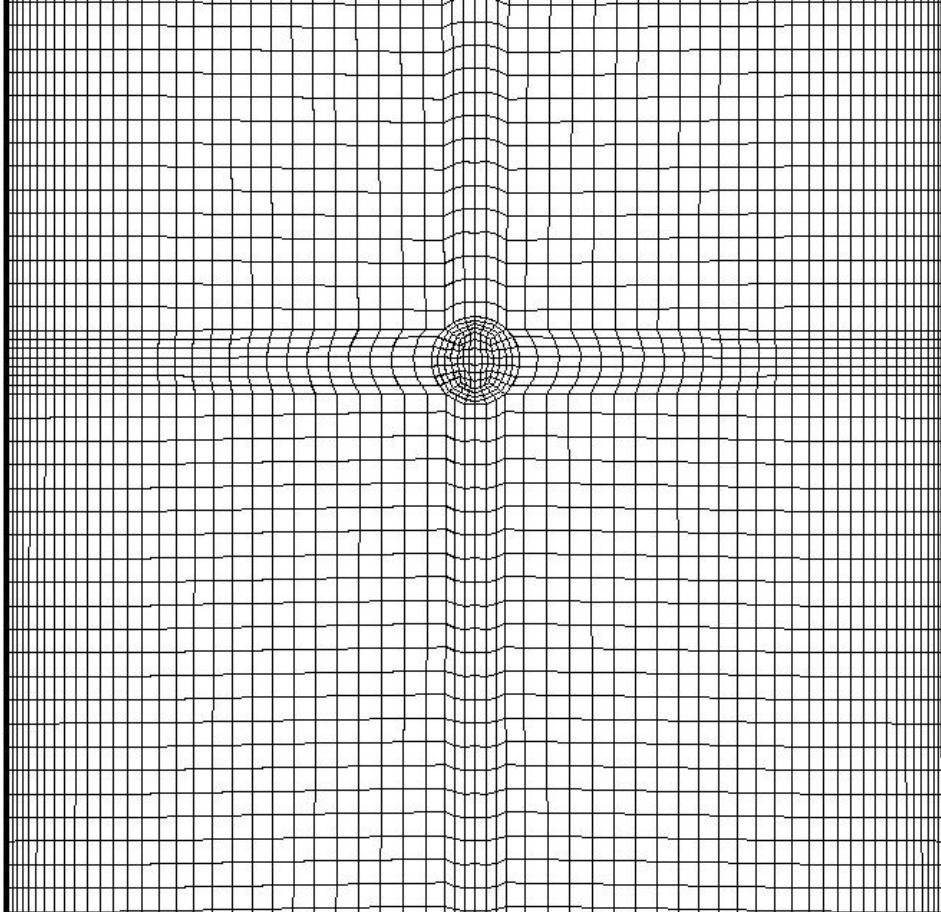


Figure D.3: Side view of the mesh

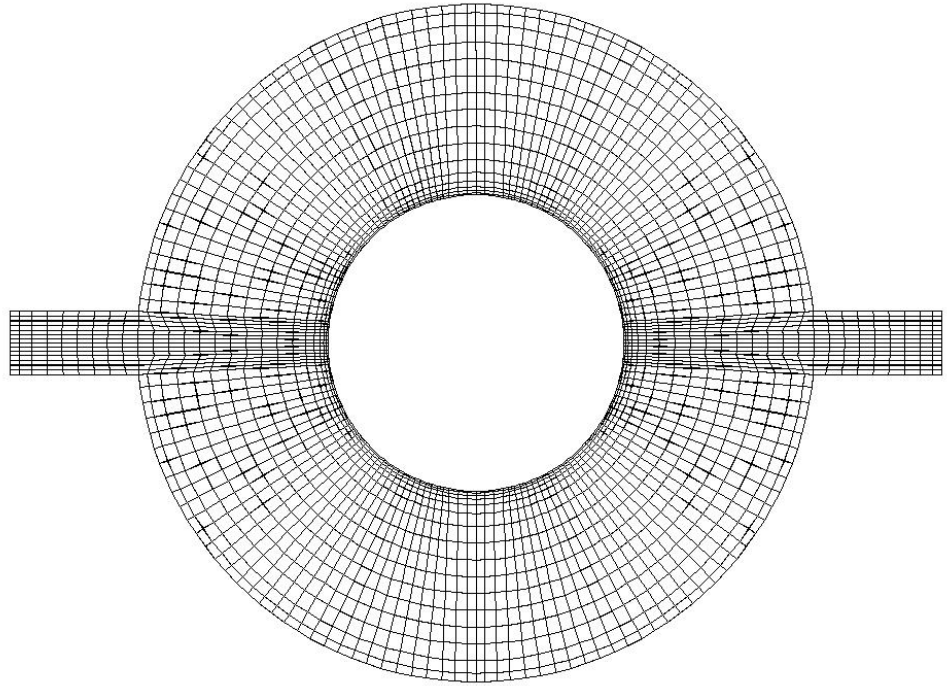


Figure D.4: Cut view of the inlets from above



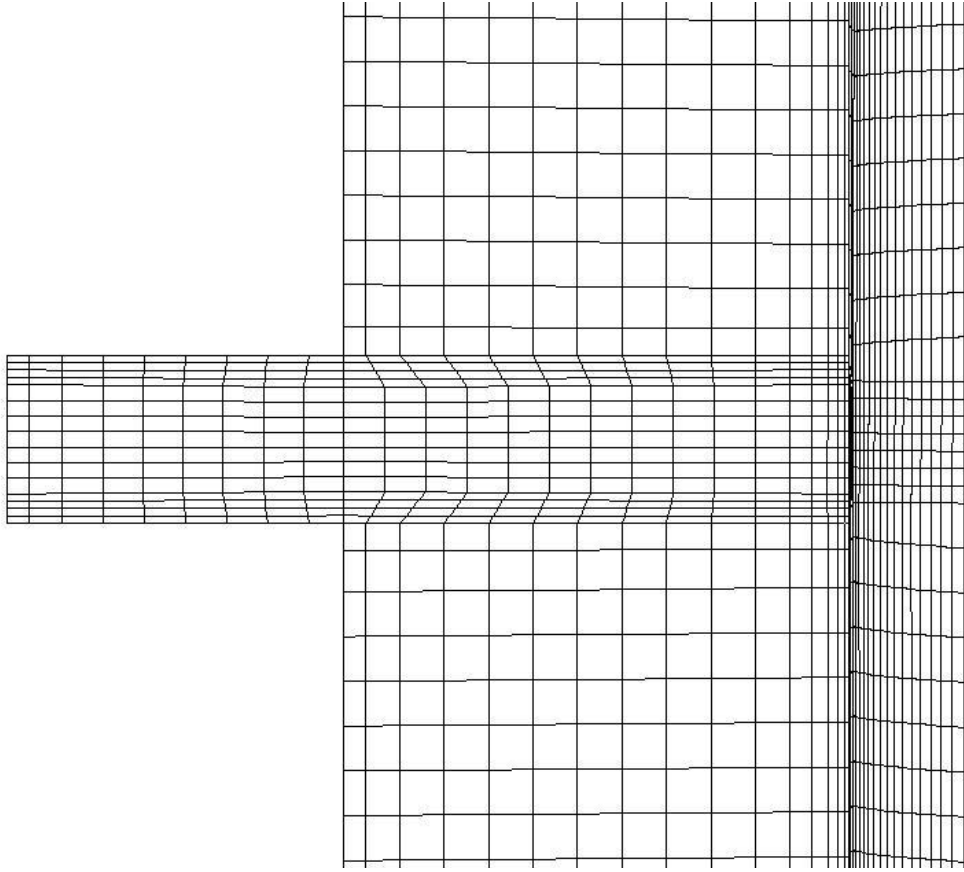


Figure D.5: Cut view of the inlet from symmetry plane (To the right inner part of the stem mesh is shown)

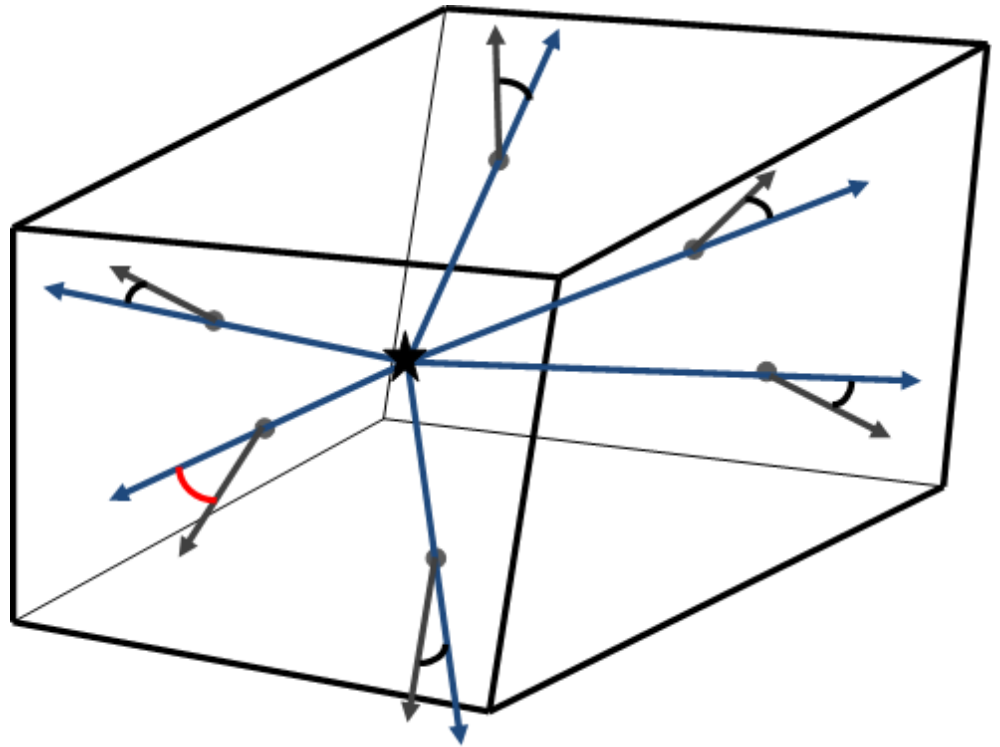


Figure D.6: Hexahedron skewness. The star represents the centroid of the hexahedron. Blue arrow is the vector from the centroid to the center of the face and gray arrow is the normal vector of the face. The red arc shows the worst possible angle between those two vectors and it has the lowest skewness.

## Appendix E

### Inlet velocity profiles

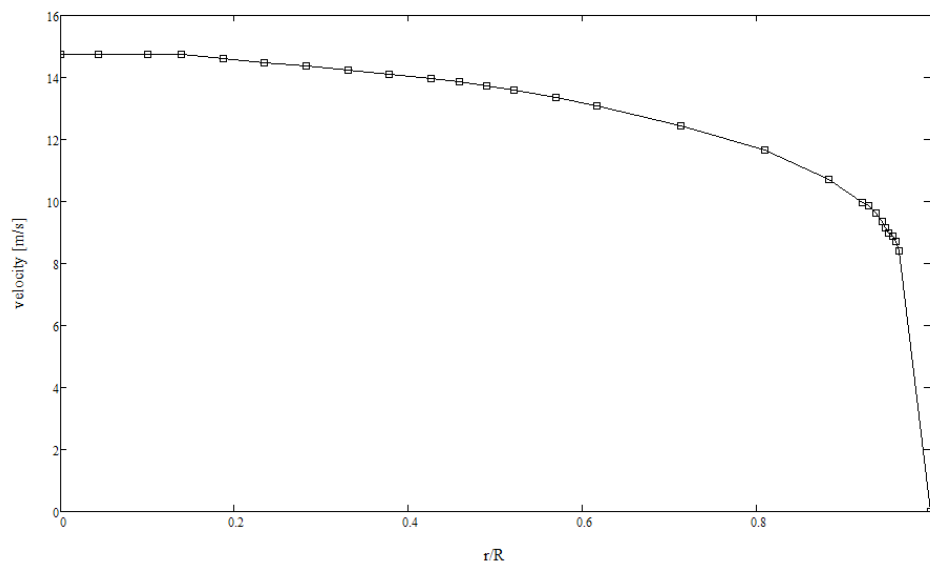


Figure E.1: Radial velocity profile for hot inlet

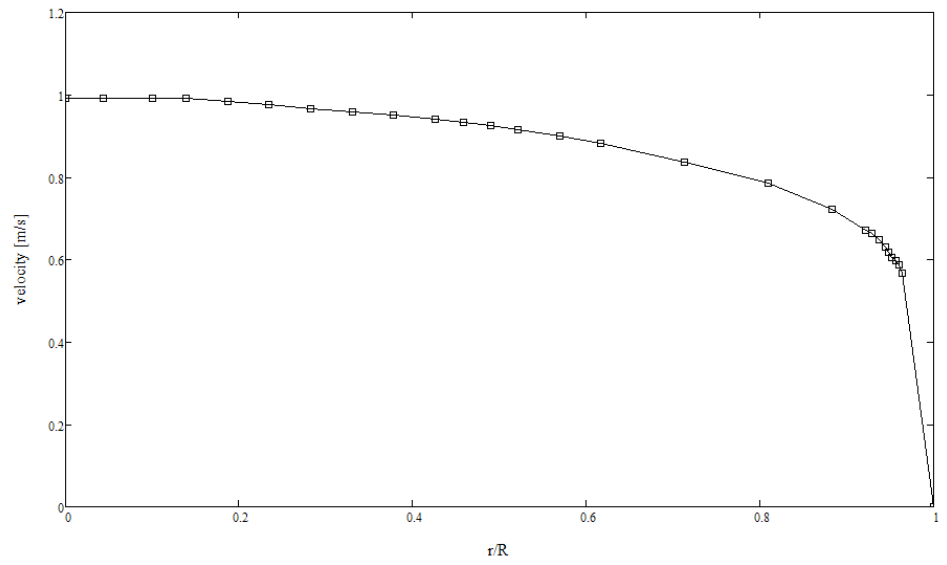


Figure E.2: Radial velocity profile for cold inlet

